nature biomedical engineering

Article

https://doi.org/10.1038/s41551-022-00978-z

Nanoparticles with ultrasound-induced afterglow luminescence for tumour-specific theranostics

Received: 22 April 2022

Accepted: 31 October 2022

Cheng Xu[1,3], Jingsheng Huang[1,3], Yuyan Jiang[1], Shasha He[1], Chi Zhang[1] & Kanyi Pu[1,2] ✉

Molecular imaging via afterglow luminescence minimizes tissue autofluorescence and increases the signal-to-noise ratio. However, the induction of afterglow requires the prior irradiation of light, which is attenuated by scattering and absorption in tissue. Here we report the development of organic nanoparticles producing ultrasound-induced afterglow, and their proof-of-concept application in cancer immunotheranostics. The 'sonoafterglow' nanoparticles comprise a sonosensitizer acting as an initiator to produce singlet oxygen and subsequently activate a substrate for the emission of afterglow luminescence, which is brighter and detectable at larger tissue depths (4 cm) than previously reported light-induced afterglow. We formulated sonoafterglow nanoparticles containing a singlet-oxygen-cleavable prodrug for the immune-response modifier imiquimod that specifically turn on in the presence of the inflammation biomarker peroxynitrite, which is overproduced by tumour-associated M1-like macrophages. Systemic delivery of the nanoparticles allowed for sonoafterglow-guided treatment of mice bearing subcutaneous breast cancer tumours. The high sensitivity and depth of molecular sonoafterglow imaging may offer advantages for the real-time in vivo monitoring of physiopathological processes.

Optical imaging allows for the close monitoring of physiopathological processes at the molecular level and is thus routinely used to decipher biology and to diagnose diseases[1–4]. To minimize autofluorescence and to improve the signal-to-background ratio (SBR), afterglow imaging uses materials (such as semiconducting polymer and rare-earth-doped inorganic nanomaterials) as the 'optical battery' to store photoenergy in defects, to then slowly release photons after the cessation of light irradiation[5–9]. With respect to enzyme-catalyzed bioluminescence and radioisotope-enabled Cerenkov imaging[10–13], afterglow imaging has the advantages of tuneable near-infrared (NIR) emission, renewable and repeatable luminescence and a long lifetime, which make the image modality useful for a variety of in vivo imaging applications, such as the ultrasensitive detection of metastatic tumours[14], intra-operative image-guided surgery[15], the real-time tracking of prodrug activation[16] and the early diagnosis of organ injuries[5].

In current implementations of afterglow imaging, despite the elimination of autofluorescence during signal acquisition, the signal-induction process requires light irradiation. Owing to light scattering and re-absorption in tissue, it is challenging to use light-induced afterglow (photoafterglow) to induce a signal in deep-seated afterglow agents[17]. This issue can potentially be addressed via the development of afterglow agents that can be induced with deep-tissue-penetrating

---

[1]School of Chemistry, Chemical Engineering and Biotechnology, Nanyang Technological University, Singapore, Singapore. [2]Lee Kong Chian School of Medicine, Nanyang Technological University, Singapore, Singapore. [3]These authors contributed equally: Cheng Xu, Jingsheng Huang. ✉e-mail: kypu@ntu.edu.sg

electromagnetic radiation. In fact, X-ray-induced afterglow has been observed from inorganic $LiGa_5O_8$:Cr@SiO_2 nanoparticles[18]. Furthermore, the emission of X-ray-induced afterglow was shifted to the second NIR range, as shown for $NaYF_4$:Er@$NaYF_4$ nanoparticles[19]. However, X-ray-induced afterglow materials are rare, and it is difficult to design probes that activate their signals only in the presence of specific biomarkers, owing to challenges in the precise control of the structure and surface modifications of the probes.

In contrast to the use of X-rays, non-radiative ultrasound is a safer deep-tissue-penetrating mechanical energy, which however has not been exploited for in vivo optical imaging[20]. Conventionally defined sonoluminescence is related to a spontaneous luminescence process from bubble cavitation after periodic expansion and extraction on ultrasound irradiation[21]. However, such sonoluminescence has a short wavelength (blue light), low brightness and extremely short lifetime (microseconds). Differently, ultrasound-triggered luminescence is an energy-releasing process from piezoelectric inorganic materials, which store photoenergy in lattice defects and radiatively release it on ultrasonic mechanical stress[22]. Recently, such piezoelectric nanoparticles were applied for sono-optogenetic stimulation of the brain through the intact mouse skull[23]. However, photocharging is a prerequisite for the ultrasound-triggered luminescence of piezoelectric nanoparticles, which precludes repeatable induction of afterglow by ultrasound application in deep tissue.

In this Article, we report organic nanoparticles that emit ultrasound-induced afterglow, and the application of such sonoafterglow for biomarker-activatable cancer immunotheranostics. Sonoafterglow nanoparticles (SNAPs) comprise a sonosensitizer as the initiator to produce singlet oxygen ($^1O_2$) under ultrasound and subsequently convert a sonoafterglow substrate into active dioxetane substrates, whose luminescence is long-lasting and able to transfer back to the sonosensitizer. The ultrasound initiation mechanism ensures the induction of sonoafterglow from deep-seated nanoparticles. Furthermore, molecular engineering of each composition allows for the development of 'smart' sonoafterglow nanoprobes that turn on their sonoafterglow signal only in the presence of specific disease biomarkers. By incorporating a macrophage-polarization prodrug into the nanoparticle, we synthesized a sonoafterglow cancer nanoimmunotheranostic probe (SCAN). SCAN activates immunotherapeutic action only under ultrasound application, emitting a sonoafterglow signal that can be coupled back to the pro-inflammatory levels of the tumour immunomicroenvironment (as characterized by the presence of M1 macrophages). Thus, SNAP serves as a modular system for deep-tissue high-contrast biomarker imaging and cancer theranostics.

Results

Development of the SNAPs

To optimize sonoafterglow, a series of sonosensitizers that generate $^1O_2$ on ultrasound application were screened for the role as sonoafterglow initiators, including rose bengal octyl ester (RB), haematoporphyrin (HMP), verteporfin (VP) and silicon 2,3-naphthalocyanine bis(trihexylsilyloxide) (NCBS) (Fig. 1a,b and Supplementary Fig. 1). Moreover, they are fluorescent agents with visible-to-NIR emission (Supplementary Fig. 2). Polymer or small molecules that can react with $^1O_2$ to produce the self-luminescence dioxetane intermediates were screened for the role as sonoafterglow substrates, including phenoxyl-adamantylidene (PA), azide-methyl acrylate-phenoxyl-adamantylidene (AMPA), poly[2-methoxy-5-(2′-ethylhexyloxy)-1,4-phenylene vinylene] (MEHPPV), dicyanomethylene-4H-benzopyran-phenoxyl-adamantylidene (DPAo) and dicyanomethylene-4H-benzothiopyran-phenoxyl-adamantylidene (DPAs) (Supplementary Fig. 3 and Table 1). SNAPs were prepared with different combinations of these sonoafterglow initiators and substrates through co-nanoprecipitation in the presence of an amphiphilic stabilizer, poly(ethylene glycol)-block-poly (propylene glycol)-block-poly (ethylene glycol) (PEG-*b*-PPG-*b*-PEG). SNAPs had the hydrodynamic diameters ranged from 50 nm to 120 nm measured by dynamic light scattering and spherical morphology detected by transmission electron microscope (TEM) (Fig. 1f and Supplementary Fig. 4).

The sonoafterglow properties of SNAPs were studied and compared for optimized composition. The optimal mass ratio between sonoafterglow initiators and substrates within SNAP was 1:5, and ultrasound application conditions were optimized to be 2.0 W cm^{-2} for 30 s (Supplementary Figs. 5–7). NCBS/AMPA SNAP had the highest sonoafterglow intensity, which was 3.1 to 243.6 times higher than other tested SNAPs (Fig. 1c,d). Furthermore, the origin of sonoafterglow emission was dependent on the spectral overlap between substrate and initiator. When the emission of sonoafterglow substrate overlaid with the absorption of initiator, energy transfer could occur, leading to the sonoafterglow emission from the initiator, for example, NCBS/MEHPPV SNAP. Otherwise, the sonoafterglow emission was dominated by the substrate, for example, RB/DPAo SNAP. The sonoafterglow half-lives for SNAPs ranged from 70 s to 180 s (for example, 110 s for NCBS/DPAs SNAP), which was long enough for in vitro and in vivo imaging (Fig. 1e). Considering the strongest sonoafterglow intensity in NIR region (peaked at 780 nm), NCBS/DPAs SNAP was chosen for the following experiments. Sonoafterglow intensities of NCBS/DPAs SNAP solutions showed no significant difference after ultrasound application for five cycles (30 s per cycle), suggesting the repeatability of sonoafterglow (Supplementary Fig. 8a). This was benefited from the low consumption rate of NCBS (~2.3%) and DPAs (~4.5%) per ultrasound application (Supplementary Fig. 8b). In addition, sonoafterglow was stably induced in different biological buffers (Supplementary Fig. 9).

Deep-tissue induction of bright sonoafterglow

To compare sonoafterglow with photoafterglow, the signal of NCBS/DPAs SNAP was acquired after ultrasound (1.0 MHz) or laser (808 nm) application for the same time (30 s). The power intensity for ultrasound was 2.0 W cm^{-2}, which was the previously optimized power intensity and within the safe range to skin (1.0–3.0 W cm^{-2}); however, laser was applied at its maximum permissive exposure (0.33 W cm^{-2}) (Fig. 2a). Under these conditions, sonoafterglow intensity was 2.4 times higher than photoafterglow, and was equal to that after laser irradiation for 90 s (Fig. 2b). To gain insight into the brighter sonoafterglow over photoafterglow, $^1O_2$ generation from NCBS under ultrasound or laser irradiation was studied. $^1O_2$ generation under ultrasound application was 1.6 times higher than that under laser irradiation for the same time (30 s) (Fig. 2c and Supplementary Fig. 10), revealing that more efficient $^1O_2$ generation was one contributor to stronger sonoafterglow signals. Under these short-time irradiation conditions (ultrasound application for 30 s or laser irradiation for 90 s), NCBS/DPAs SNAP had no detectable cytotoxicity (Fig. 2d). This could be attributed to the $^1O_2$-scavenging effect by the afterglow substrates inside nanoparticles. However, after long-term ultrasound application (5 min), NCBS/DPAs SNAP induced 90% of cancer cell death, which was 1.6 times higher than that under laser irradiation for the same time. To study the cavitation effect on cell viability, SNAP without NCBS (SNAPc) was incubated with cancer cells followed by ultrasound application. SNAPc and SNAP at same concentration caused 19.8 ± 3.9% and 84.9 ± 4.7% of 4T1 cancer cell death, respectively, suggesting that cavitation played a minor role in cell viability (Supplementary Fig. 11). In addition, $^1O_2$ generation from SNAP upon ultrasound application was ~216 times higher than other reactive oxygen species, including ·OH and $O_2^{\cdot-}$, revealed by electron spin resonance (ESR) spectroscopy (Supplementary Fig. 12). These findings verified that tumour cell killing was mainly attributed to sonodynamic effect from sonosensitizer in SNAPs. Overall, such an application time-dependent ultrasound toxicity enabled safe sonoafterglow imaging (short term, 30 s) and sonodynamic tumour killing (long term, 5 min).

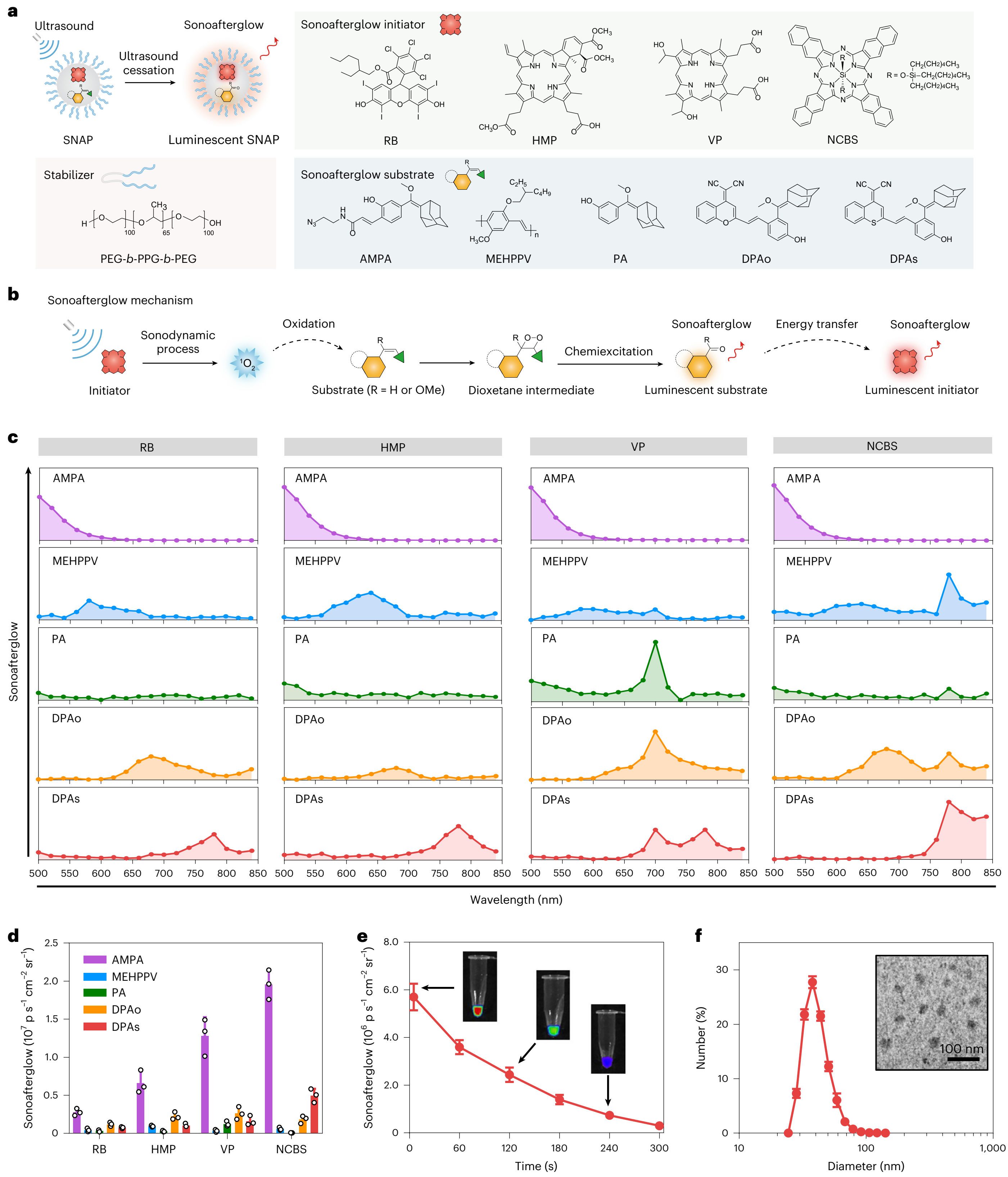

Fig. 1 | Screening and optimization of SNAPs. a, Schematic illustration for sonoafterglow imaging and components for SNAPs including sonoafterglow initiators, substrates and stabilizers. **b**, Molecular mechanism of sonoafterglow. Under ultrasound application, initiators produce $^1O_2$ to convert sonoafterglow substrate into active dioxetane substrates that slowly decompose and emit afterglow luminescence. The luminescence can transfer back to sonosensitizer and re-emit at longer wavelength. **c**,**d**, Sonoafterglow spectra (**c**) and intensities (**d**) of SNAPs with different compositions ([afterglow substrate] = 20 μg ml^{-1}). Sonoafterglow spectra were acquired using IVIS bioluminescence mode with specific emission filters (acquisition time 1 s per filter) after ultrasound application at 2.0 W cm^{-2} for 30 s. Sonoafterglow intensities were measured using IVIS under same condition yet with open filter (acquisition time 1 s). **e**, Sonoafterglow decay of NCBS/DPAs SNAP ([DPAs] = 20 μg ml^{-1}). Acquisition time: 1 s. **f**, Size distribution and representative TEM image of NCBS/DPAs SNAP ([DPAs] = 10 μg ml^{-1}). For all experiments, $n = 3$ independent samples. Data are presented as mean ± s.d.

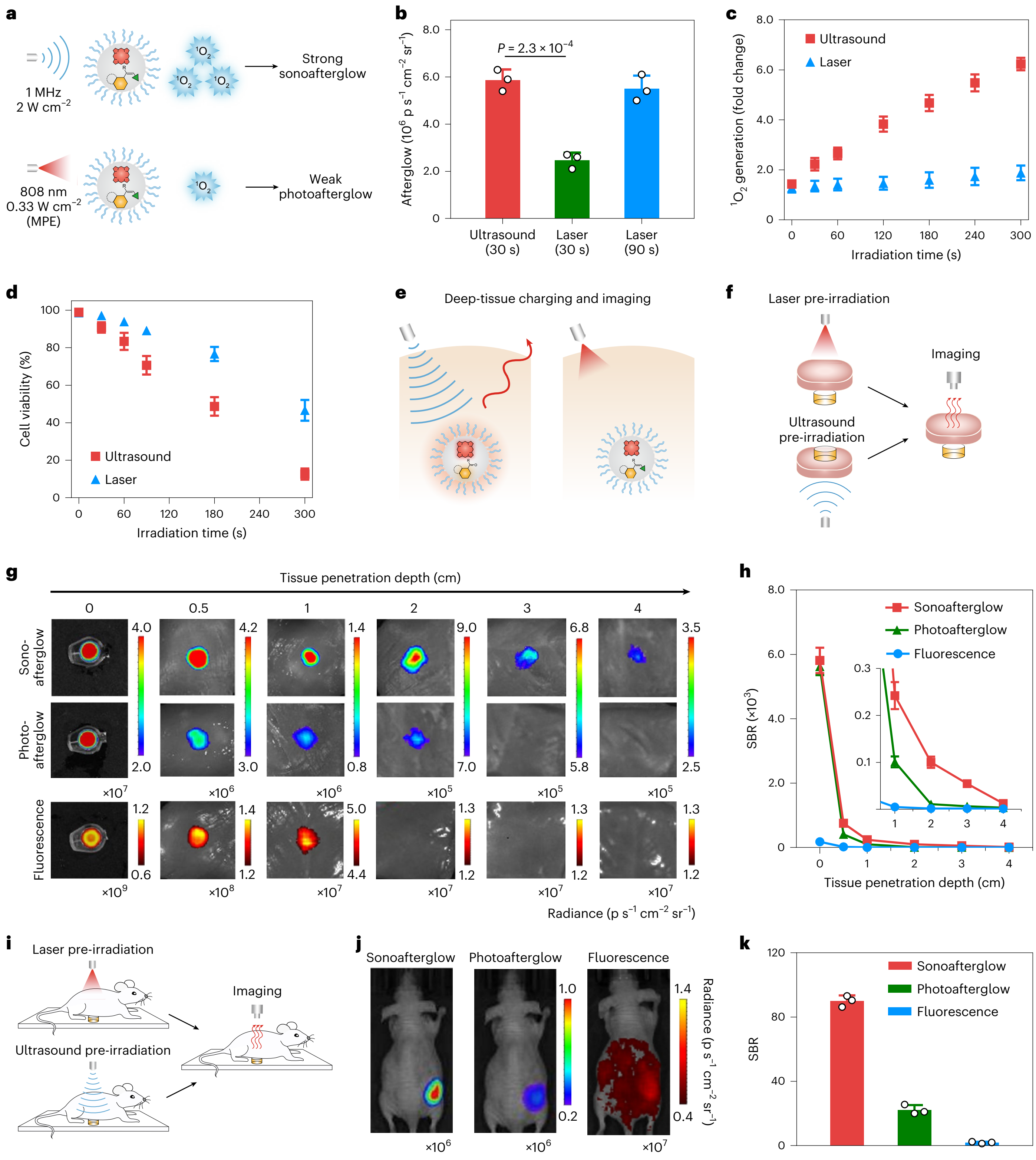

Fig. 2 | Deep-tissue induction of sonoafterglow. a, Schematic illustration comparing sonoafterglow and photoafterglow. MPE: maximum permissive exposure. **b**, Afterglow intensities of NCBS/DPAs SNAP ([DPAs] = 20 μg ml^{-1}) under ultrasound or laser irradiation for indicated time. Acquisition time: 1 s. **c**, $^1O_2$ generation of NCBS/DPAs SNAP ([DPAs] = 20 μg ml^{-1}) under ultrasound or laser irradiation over time. **d**, Viability of 4T1 cancer cells treated with NCBS/DPAs SNAP ([DPAs] = 20 μg ml^{-1}) after ultrasound or laser irradiation over time (*n* = 3 independent samples). **e**, Schematic illustration comparing sonoafterglow and photoafterglow of SNAPs in deep tissue. **f**, Schematic illustration showing the induction and detection of afterglow from SNAPs through chicken breast tissues. **g**,**h**, Representative images (**g**) and SBRs (**h**) for sonoafterglow, photoafterglow and fluorescence of NCBS/DPAs SNAP ([DPAs] = 100 μg ml^{-1}) induced and detected through chicken breast tissue of different thickness. **i**, Schematic illustration showing the induction and detection of afterglow from SNAPs through a living mouse. **j**,**k**, Representative images (**j**) and SBRs (**k**) for sonoafterglow, photoafterglow and fluorescence of NCBS/DPAs SNAP ([DPAs] = 100 μg ml^{-1}) through a living mouse (~1.8 cm tissue depth). In **g** and **j**, acquisition time for sonoafterglow and photoafterglow: 1 s; acquisition time for fluorescence: 0.1 s. Ultrasound settings: 1.0 MHz, 100 Hz, 50% duty, 2.0 W cm^{-2}, 30 s. Laser settings: 808 nm, 0.33 W cm^{-2}, 90 s. For all experiments, *n* = 3 independent samples. Data are presented as mean ± s.d. Statistical significance was calculated via one-way ANOVA followed by Tukey's post hoc test (**b**).

To study how deep sonoafterglow could be induced and detected in tissue, NCBS/DPAs SNAP solution was covered with chicken breast tissues, followed by ultrasound application or laser irradiation through the tissues before signal detection (Fig. 2e,f). To rule out the effect of intensity difference on tissue penetration depth, ultrasound application ($2.0\ \mathrm{W\ cm^{-2}}$ for 30 s) and NIR laser irradiation ($0.33\ \mathrm{W\ cm^{-2}}$ for 90 s) were conducted to afford the same level of afterglow intensities. Owing to the minimized background noise, SBRs for sonoafterglow and photoafterglow were higher than NIR fluorescence at all tissue depths (Fig. 2g,h). Particularly, sonoafterglow was induced and clearly detected even at the tissue depth of 4 cm (SBR 12.5). By contrast, photoafterglow and NIR fluorescence were hardly detectable above the tissue depth of 2 cm (SBR 11.1) and 1 cm (SBR 5.14), respectively. When NCBS/DPAs SNAP solution was pre-irradiated by ultrasound or laser without chicken breast coverage, and signals were detected through chicken breast, SBRs for sonoafterglow and photoafterglow were similar at all tissue depths (Supplementary Fig. 13). These data confirmed that the better performance of sonoafterglow in the former penetration experiment was attributed to deeper tissue penetration of ultrasound relative to laser. This advantage was further observed through a living mouse (~1.8 cm tissue depth) (Fig. 2i–k), showing that sonoafterglow SBR was 4.0 and 47.4 times higher than that for photoafterglow and fluorescence, respectively. These data confirmed the superiority of sonoafterglow over photoafterglow in induction and imaging of deep-seated nanoparticles.

Biomarker-activatable sonoafterglow imaging

A pro-inflammatory microenvironment status plays a crucial role in the onset and progression of tumours, and therefore it can serve as a prognostic signature for cancer immunotherapy[24]. Despite the importance of molecular imaging in cancer diagnosis and therapy, a majority of existing imaging agents have ‘always-on’ signals and produce non-specific signals on passive accumulation[25]. To enable the correlation of the signal with the pro-inflammatory status of the tumour microenvironment, we developed an activatable molecular sonoafterglow probe (which we named SNAP-M) based on NCBS/DPAs SNAP (Fig. 3a,b and Supplementary Fig. 14). Peroxynitrite ($ONOO^-$) was chosen as the biomarker for pro-inflammatory tumour microenvironment, which was reported to correlate with positive prognosis of immunotherapy[26]. $ONOO^-$ is overproduced by tumour-associated M1-like macrophages (M1 macrophages) via the reaction between nitric oxide (NO, the product of iNOS: inducible nitric oxide synthase) and superoxide anion ($O_2^{\cdot-}$, the product of mitochondrial electron transfer chain) and extensively distributed in tumour microenvironment[27] (Supplementary Fig. 15). $ONOO^-$ exerts direct tumour-killing effects and promotes other immune-activating factors to inhibit tumour angiogenesis and suppress metastatic niche formation, which endows M1-macrophage with anti-tumour phenotype that is in sharp contrast to pro-tumoural M2 macrophages[28]. Different from NCBS/DPAs SNAP, SNAP-M comprised a silenced DPAs caged with $ONOO^-$ responsive moiety (Pro-DPAs)[29] (Supplementary Fig. 16). Thus, the sonoafterglow of SNAP-M could be specifically activated by the highly upregulated $ONOO^-$ in M1-characterized pro-inflammatory tumour microenvironment. Meanwhile, the ‘always-on’ NCBS fluorescence was used to track the location of SNAP-M. To study the detection selectivity of SNAP-M, sonoafterglow was detected after incubation with different reactive oxygen and nitrogen species (RONS) and metal ions (Fig. 3c,d). The sonoafterglow of SNAP-M increased by 140-fold after incubation with $ONOO^-$ but remained nearly unchanged for other RONS, including hypochlorite (ClO^-), superoxide anion ($O_2^{\bullet-}$), hydroxyl radicals (•OH), hydrogen peroxide (H_2O_2) and nitric oxide (NO), and metal ions, including calcium ion (Ca^{2+}) and ferrous ion (Fe^{2+}). Moreover, the sonoafterglow of SNAP-M had a good linearity with $ONOO^-$ concentration, showing a limit of detection (LOD) down to $0.3\ \mu M$ (Supplementary Fig. 17).

The sonoafterglow turn-on specificity of SNAP-M towards M1 macrophages was studied in vitro. M1 macrophages were differentiated from Raw 264.7 cells (M0 macrophages) after treatment with M1-polarizing factors (LPS: lipopolysaccharides and IFN-γ: interferon-γ)[30], which were verified by M1-characteristic morphology and the upregulated iNOS (Supplementary Fig. 18). The detection of sonoafterglow was conducted after incubating SNAP-M with various cells, including M1, M2, M0 macrophages, 4T1 cancer cells or NIH 3T3 fibroblasts, for 12 h (Supplementary Fig. 19). The fluorescence intensities from NCBS were same for all tested cells, suggesting the comparable cellular uptake of SNAP-M. However, the sonoafterglow of SNAP-M was the strongest in M1 macrophages, showing ~5.0 times brighter sonoafterglow than that in M0 and M2 macrophages (Fig. 3e,f). Furthermore, the sonoafterglow in M1 macrophages dramatically decreased to the basal level upon pre-treatment of $ONOO^-$ scavenger, *N*-acetylcysteine.

To validate the signal correlation of SNAP-M with the level of intra-tumoural M1 macrophage during immunotherapy, SNAP-M was intravenously injected into 4T1 tumour-bearing mice after treatment with saline or M1-oriented macrophage-polarizing agent resquimod (R848) (refs. [31,32]) (Fig. 3g). At 36 h post-injection of SNAP-M, the NIR fluorescence from NCBS reached maximum for both groups, suggesting the highest accumulation of SNAP-M (Supplementary Fig. 20). At this timepoint, the tumour sonoafterglow intensity for R848-treated mice was 3.5 times higher than that for saline-treated mice, with the SBR as high as 72.2 (Fig. 3h,i). Furthermore, the SBR of sonoafterglow was 2.5 times higher than photoafterglow (irradiated by 808 nm laser) for R848-treated mice. Flow cytometry confirmed that M1 macrophage population in R848-treated mice was 9.5 times higher than that in saline-treated mice (Fig. 3j). Thereby, these data not only confirmed that enhanced sonoafterglow for R848 treatment group was correlated with increased tumour M1 macrophage population, but also revealed the superiority of sonoafterglow over photoafterglow in in vivo imaging.

To study the deep-tissue imaging capability of SNAP-M against M1-characterized pro-inflammatory tumour microenvironment, sonoafterglow imaging was conducted by induction and detection through chicken breast tissues with increased thickness. At 2 cm thickness, $ONOO^-$-activated sonoafterglow was induced and detected with a SBR of 13.3, which was not possible for photoafterglow and fluorescence (Fig. 3k,l). These results verified the higher sensitivity of deep-tissue sonoafterglow of SNAP-M over photoafterglow for the monitoring of M1-characterized pro-inflammatory tumour microenvironment.

Cancer immunotheranostics via sonoafterglow

Despite the promise of immunotherapy in cancer treatment, patient response varies among cancer types and even within cohorts with the same malignancy, leading to either treatment failure or overdose-related toxicity[33,34]. As the response rates and therapeutic outcome have been revealed to closely associate with the pro-inflammatory tumour microenvironment[35,36], cancer immunotherapeutic agents that can send real-time feedback information on pro-inflammatory tumour microenvironment are highly desired to guide treatment regimens. To achieve such precision cancer immunotherapy, SCAN was developed to comprise not only a silenced sonoafterglow initiator, Pro-MB: a methylene blue (MB) derivative caged with a $ONOO^-$-cleavable moiety, but also an M1-polarizing prodrug, Pro-R837: an imiquimod (R837) derivative caged with a $^1O_2$-cleavable moiety (Fig. 4a,b and Supplementary Figs. 21 and 22). Only in the presence of high level of $ONOO^-$ in the pro-inflammatory tumour microenvironment was the sonoafterglow initiator activated to generate sonodynamic effect (production of $^1O_2$), consequently leading to the sonoafterglow from the substrate AMPA for feedback; additionally, the generated $^1O_2$ resulted in the cleavage of imiquimod from Pro-R837 for in situ activation of immunotherapy. As designed, SCAN intrinsically showed negligible fluorescence, $^1O_2$ generation under ultrasound

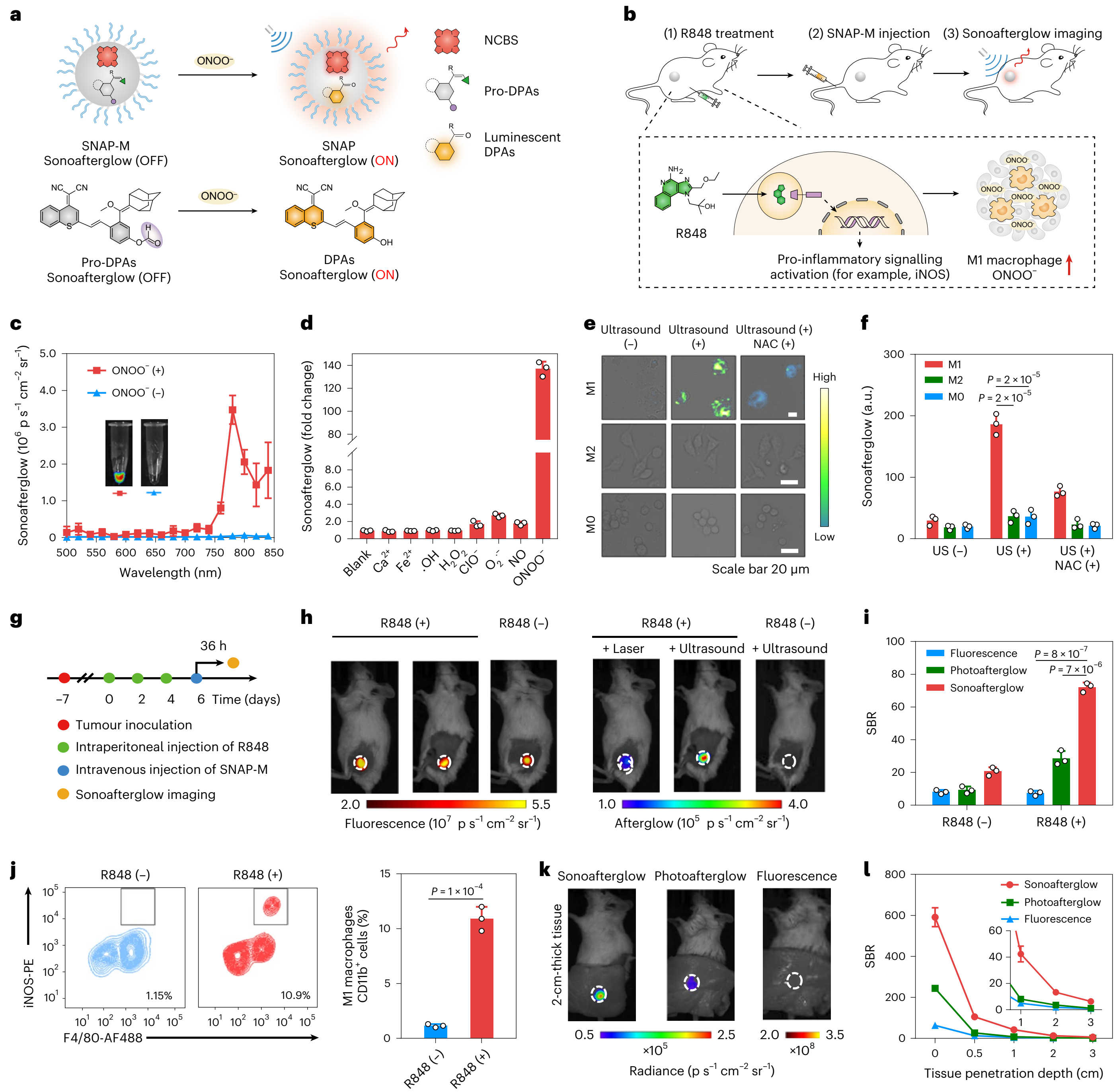

Fig. 3 | Activatable sonoafterglow imaging of M1 macrophages. **a**, Molecular mechanism of SNAP-M for activatable sonoafterglow imaging of M1-characterized pro-inflammatory tumour microenvironment. ONOO$^-$ overproduced in pro-inflammatory tumour microenvironment activates Pro-DPAs to DPAs to emit sonoafterglow after ultrasound application. **b**, Scheme of R848-induced M1-characterized pro-inflammatory tumour microenvironment monitored by sonoafterglow imaging in vivo. Sonoafterglow imaging was applied to the tumours of mice treated with R848 to induce highly pro-inflammatory tumour condition featured by M1 macrophage and ONOO$^-$. **c**, Sonoafterglow spectra of SNAP-M ([Pro-DPAs] = 40 μM) with or without incubation with ONOO$^-$ (80 μM). Ultrasound settings: 2.0 W cm^{-2}, 30 s. Acquisition time: 1 s per filter. **d**, Sonoafterglow fold change of SNAP-M ([Pro-DPAs] = 40 μM) after incubation with different RONS (80 μM) or metal ions (100 μM). Ultrasound settings: 2.0 W cm^{-2}, 30 s. Acquisition time: 1 s. **e**,**f**, Microscopic images (**e**) and intensities (**f**) of sonoafterglow in M0, M1 and M2 macrophages after incubation with SNAP-M ([Pro-DPAs] = 20 μg ml^{-1}) for 12 h. Ultrasound settings: 2.0 W cm^{-2}, 30 s. Acquisition time: 5 s. NAC, N-acetylcysteine. **g**, Timetable for sonoafterglow imaging on saline- or R848-treated 4T1 tumour-bearing mice after intravenous injection of SNAP-M. **h**,**i**, Representative images (**h**) and SBRs (**i**) for fluorescence, photoafterglow and sonoafterglow on tumours from saline- or R848-treated mice at 36 h after intravenous injection of SNAP-M ([Pro-DPAs] = 250 μg ml^{-1}, 200 μl). **j**, Flow-cytometric plots and quantification of tumour M1 macrophages (F4/80$^+$iNOS^{high}) in CD11b$^+$ cells at day 8. **k**,**l**, Representative images (**k**) and SBRs (**l**) for fluorescence, photoafterglow and sonoafterglow on tumours from mice intra-tumourally injected with SNAP-M ([Pro-DPAs] = 50 μg ml^{-1}, 50 μl). For **h** and **k**, sonoafterglow was acquired for 10 s after ultrasound application (2.0 W cm^{-2}) for 30 s; photoafterglow was acquired for 10 s after laser irradiation (808 nm, 0.33 W cm^{-2}) for 90 s, and fluorescence was captured for 0.1 s (Ex = 710 nm, Em = 780 nm). For all experiments, *n* = 3 independent samples or animals. Data are presented as mean ± s.d. Statistical significance was calculated via one-way ANOVA followed by Tukey's post hoc test (**f** and **i**) or two-tailed Student's *t*-test (**j**).

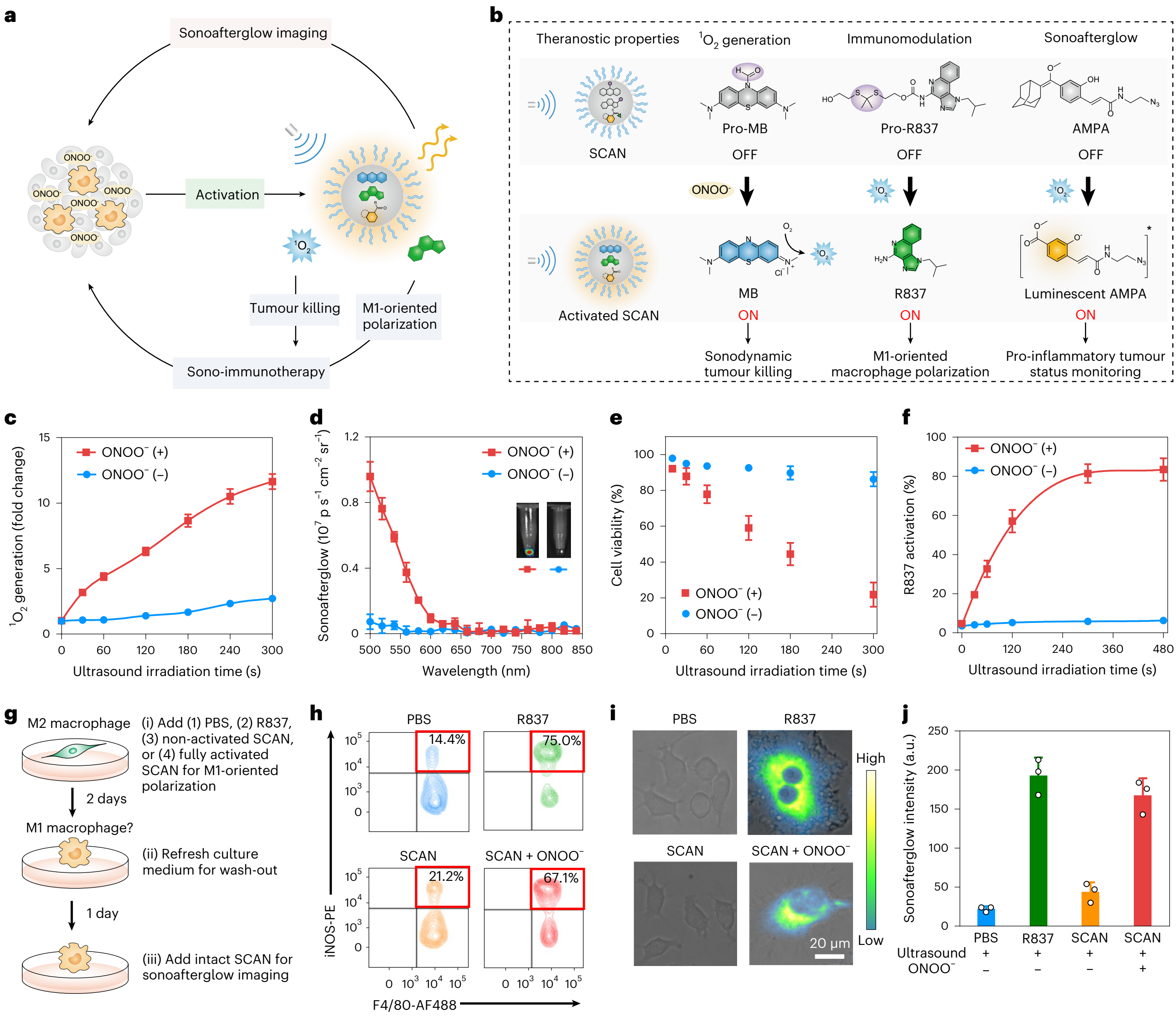

Fig. 4 | Sonoafterglow cancer immunotheranostics in vitro. a, Scheme of SCAN for sonoafterglow-guided cancer immunotherapy. SCAN is activated by ONOO$^-$ in tumour microenvironment for sonoafterglow imaging of M1-characterized pro-inflammatory environment; in turn, activated SCAN exerts sono-immunotherapy to kill tumour cells and elicit M1 macrophages, producing more ONOO$^-$ for SCAN activation. **b**, Molecular mechanism of SCAN for sonoafterglow cancer nano-immunotheranostics. Sonoafterglow initiator is activated by ONOO$^-$ in tumour microenvironment to generate sonodynamic effect (production of $^1O_2$), causing sonoafterglow from the substrate AMPA for feedback and liberating imiquimod from Pro-R837 for in situ activation of immunotherapy. **c**, $^1O_2$ generation of Pro-MB (30 μM) before and after treatment with ONOO$^-$ (60 μM) upon ultrasound application (2.0 W cm^{-2}) over time. **d,** Sonoafterglow spectra of SCAN ([Pro-MB] = 30 μM) before and after treatment with ONOO$^-$ (60 μM). Ultrasound settings: 2.0 W cm^{-2}, 30 s. Acquisition time: 1 s per filter. **e**, Viability of 4T1 cancer cells treated with ONOO$^-$ (60 μM) activated or non-activated SCAN ([Pro-MB] = 30 μM) upon ultrasound application (2.0 W cm^{-2}) over time. **f**, Kinetics of Pro-R837 activation in SCAN ([Pro-MB] = 30 μM) in the presence or absence of ONOO$^-$ (60 μM) upon ultrasound application (2.0 W cm^{-2}) over time. **g**, Procedures for M1 polarization and sonoafterglow signal feedback of SCAN in macrophages. SCAN was treated with ONOO$^-$ (60 μM) and irradiated with ultrasound (2.0 W cm^{-2}) to be fully activated. **h**, Flow-cytometric plots of M1 macrophages (F4/80$^+$iNOS^{high}) after incubation with saline, free imiquimod (R837), non-activated SCAN (ultrasound-irradiated only) and fully activated SCAN for M1 polarization. [Pro-R837] = 10 μg ml^{-1}. **i**,**j**. Microscopic images (**i**) and intensities (**j**) of sonoafterglow from macrophages (after indicated treatments) incubated with fresh intact SCAN ([Pro-MB] = 30 μM). Ultrasound settings: 2.0 W cm^{-2}, 30 s. Acquisition time: 1 s. For all experiments, *n* = 3 independent samples. Data are presented as mean ± s.d. Statistical significance was calculated via one-way ANOVA followed by Tukey's post hoc test (**j**).

application and sonoafterglow, because MB was in caged form (Fig. 4c,d and Supplementary Fig. 23). After ONOO$^-$ addition, SCAN increased its fluorescence by 95.1-fold, $^1O_2$ generation by 4.4-fold and sonoafterglow by nearly 80-fold. However, no significant changes were observed by other tested RONS and metal ions (Supplementary Fig. 24). The sonoafterglow intensity of SCAN correlated well with ONOO$^-$ concentration with an LOD of 0.1 μM, which was two times lower than fluorescence LOD. Moreover, non-activated SCAN did not cause 4T1 cancer cell death upon ultrasound application; in contrast, ONOO$^-$-activated SCAN led to 78.1% of 4T1 cancer cell death after ultrasound application for 5 min (Fig. 4e). This indicated that the potent sonodynamic tumour killing by SCAN was specifically activated in the presence of ONOO$^-$.

The $ONOO^-$ and ultrasound dual-locked activation of immunotherapeutic action for SCAN was studied in vitro. In the absence of $ONOO^-$, even after ultrasound application of SCAN, the elution peak related to free imiquimod (retention time $T_R = 10.5$ min) was hardly observed in high-performance liquid chromatography (HPLC). Only when SCAN was pre-treated with $ONOO^-$ was the imiquimod peak clearly shown after ultrasound application and enhanced over time, ultimately achieving a high activation level of Pro-R837 up to 83.5% (Fig. 4f and Supplementary Fig. 24). The theranostic ability of SCAN was studied by treating M2 macrophages with fully activated SCAN (pre-activated with $ONOO^-$ and pre-irradiated with ultrasound), followed by addition of intact SCAN for correlation of sonoafterglow with M1-oriented macrophage polarization (Fig. 4g). The fully activated SCAN repolarized M2 macrophages to M1 macrophages to the level similar to free R837, eliciting 4.4 and 3.1 times higher M1 macrophages population than PBS and non-activated SCAN (only pre-irradiated with ultrasound), respectively (Fig. 4h). Next, intact SCAN was added into all groups for sonoafterglow detection. The sonoafterglow intensity in fully activated SCAN-treated cells was 7.6 and 3.8 times higher than PBS and non-activated SCAN (Fig. 4i,j and Supplementary Fig. 25). Thereby, these data verified that SCAN had the potential to act as a dual-locked smart theranostic agent that allowed for precise M1-polarizing immunotherapy and sonoafterglow readout of therapeutic outcomes.

To demonstrate the precision immunotheranostic capability of SCAN in vivo, a theranostic regimen was proposed and tested in the subcutaneous 4T1 tumour-bearing mice (Fig. 5a,b). SCAN-C (SCAN without Pro-R837) was set as control. First, SCAN was systemically administered. At the optimal tumour accumulation of SCAN (day 0.5) indicated by NIR fluorescence from MB (Supplementary Figs. 26–28), sonoafterglow was detected for evaluation of tumour-intrinsic M1-characterized pro-inflammatory level, followed by long-term ultrasound application (5 min) to induce the $^1O_2$ generation and activation of Pro-R837 from SCAN for M1 macrophage-polarizing sono-immunotherapy (according to the kinetics of $^1O_2$ generation and Pro-R837 activation in vitro; Fig. 4c,f). At day 2, sonoafterglow signal was back down to the baseline level owing to the consumption of SCAN components, suggesting that multiple doses of SCAN were required. Therefore, a fresh dose of SCAN was administered, and sonoafterglow was detected and compared with that of the previous SCAN dose. The difference in the sonoafterglow intensities of sequential SCAN imaging was defined as ΔS and used to correlate with the increased level of M1-characterized pro-inflammatory status of tumour after each treatment. These steps were repeated to form a theranostic cycle, allowing for close monitoring of the immunotherapeutic outcome of SCAN. Compared with that after the first dose (day 0), sonoafterglow intensity showed a 4.82-fold increase after the second dose (day 2, $\Delta S = 3.0 \times 10^5$ ps^{-1} cm^{-2} sr^{-1}, $P < 0.001$), which further showed a 1.74-fold increase after the third dose (day 4, $\Delta S = 2.8 \times 10^5$ ps^{-1} cm^{-2} sr^{-1}, $P < 0.001$) (Fig. 5c–e and Supplementary Fig. 29). These suggested the improvement of tumour pro-inflammatory condition by three doses of SCAN, which might be associated with the enhanced M1 macrophage population. However, ΔS had no significant statistical difference after the fourth dose ($\Delta S = 2.8 \times 10^4$ ps^{-1} cm^{-2} sr^{-1}, $P > 0.05$), suggesting that SCAN might no longer improve the pro-inflammatory tumour microenvironment; therefore, such a theranostic regimen was discontinued. Consequently, SCAN + ultrasound therapy induced 1.8 and 3.3 times higher sonoafterglow intensities relative to SCAN-C + ultrasound therapy and SCAN groups at day 8, which suggested a higher level of M1-oriented macrophage polarization by combinational sonodynamic immunotherapy (SCAN + ultrasound).

To validate that sonoafterglow intensity was correlated with intra-tumoural M1 macrophages, tumour immune microenvironment was analyzed after theranostic regimen discontinued at day 8. Without ultrasound application, SCAN did not elicit M1 macrophages just as saline, because Pro-R837 was inactive. Ultrasound application of SCAN (for 5 min) elicited 6.4 times more M1 macrophages than saline (Fig. 5f and Supplementary Fig. 30). Ultrasound application of SCAN-C (for 5 min) also increased M1 macrophage population even without Pro-R837, because sonodynamic therapy alone induced tumour immunogenic cell death, as verified by the significant cytosol translocation of high mobility group box 1 (HMGB-1) and cell surface exposure of calreticulin (Supplementary Fig. 31). Superior to SCAN-C, SCAN elicited 2.8 times more of M1 macrophages under same ultrasound application, which was attributed to the synergistic sono-immunotherapeutic effects. Importantly, the trend of increase in M1 macrophage populations coincided with sonoafterglow signals in each group. SCAN-mediated sono-immunotherapy increased tumour-infiltrating mature dendritic cells (DCs) and cytotoxic T cells (CTLs) by 6.5- and 4.4-fold and decreased immunosuppressive regulatory T cells (T_{Reg} cells) by 1.9-fold compared with saline (Fig. 5g–i and Supplementary Figs. 32–34); it also substantially increased the level of intra-tumoural tumouricidal cytokines, including interleukin-12 (IL-12) and IFN-γ, and decreased the level of immunosuppressive cytokines, including tumour growth factor-β (TGF-β) and IL-10 (Supplementary Fig. 35).

The effect of SCAN-mediated sono-immunotherapy on tumour progression was further studied. SCAN itself did not inhibit tumour growth; however, upon long-term ultrasound application, SCAN achieved tumour eradication, prevented tumour recurrence and improved the overall survival of mice within 3 weeks (Fig. 5j,k). By contrast, SCAN-C-mediated mono-sonodynamic therapy failed to eliminate tumour, and the accelerated tumour growth was observed after 2 weeks. Furthermore, metastatic nodule was not found in lungs of mice treated with SCAN-mediated sono-immunotherapy (Fig. 5l,m), which was not achieved by other groups. To test whether SCAN could induce durable immune responses, mice that survived SCAN + ultrasound therapy were rechallenged with subcutaneously injected 4T1 cancer cells (Fig. 5n,o). Mice that received the previous SCAN + ultrasound therapy showed no tumour growth and improved overall survival compared with the untreated mice. The efficient inhibition of SCAN + ultrasound-treated mice on rechallenged tumour could be ascribed to the anti-tumour immunological memory of memory T cells[37], which derived from effector T cells that encountered tumour-associated antigens triggered by SCAN-mediated sonodynamic immunotherapy. This was validated by the fact that the population of central memory CTLs ($CD8^+CD44^{high}CD62L^{high}$) in spleens from SCAN + ultrasound therapy-treated mice were 2.5 times higher than that from untreated mice (Supplementary Fig. 36). These results confirmed that SCAN-mediated sono-immunotherapy induced potent

Fig. 5 | In vivo sonoafterglow cancer theranostics. a, Theranostic regimen of SCAN-mediated sonoafterglow cancer theranostics. **b**, Timetable of sonoafterglow-guided cancer sono-immunotherapy on 4T1 tumour-bearing mice. **c**,**d**, Representative images (**c**) and intensities (**d**) of sonoafterglow on tumours before and at 0.5 h after SCAN-C or SCAN ([AMPA] = 250 μg ml^{-1}, 200 μl) administration ($n = 3$ mice). Sonoafterglow images were acquired for 10 s after ultrasound application (2.0 W cm^{-2}) for 30 s. **e**, ΔS and statistic difference of sonoafterglow between the sequential doses ($n = 3$ mice). **f**–**i**, Flow-cytometric quantification of intra-tumoural M1 macrophage ($CD11b^+F4/80^+iNOS^{high}$) (**f**), DCs ($CD11c^+CD80^+CD86^+$) (**g**), CTLs ($CD3^+CD8^+$) (**h**) and T_{Reg} cells ($CD4^+Foxp3^+$) (**i**) at day 8 after indicated treatments ($n = 3$ mice). **j**,**k**, Tumour growth curves (**j**) and survival curves (**k**) of mice after indicated treatments ($n = 6$ mice). **l**,**m**, Quantification of pulmonary metastatic nodules (**l**) and representative H&E-stained lung section images (**m**) of mice at day 14 after indicated treatments. **n**,**o**, Tumour growth curves (**n**) and survival curves (**o**) of SCAN + ultrasound therapy-treated mice after subcutaneously re-inoculation of 4T1 cancer cells ($n = 6$ mice). Data are presented as mean ± s.d. Statistical significance was calculated via two-tailed Student's *t*-test or one-way ANOVA followed by Tukey's post hoc test (**e**–**l** and **n**–**o**).

and long-lasting immunological memory against tumour progression and recurrence.

To study the biodistribution of SCAN, tumour and main organs were collected from 4T1 tumour-bearing mice at 12 h after intravenous injection, and their SCAN contents were determined on the basis of MB fluorescence. The fluorescence intensities of tumours were over 1.5 times higher than those of other organs (Supplementary Fig. 37), suggesting SCAN activation in tumour. For measurement, all tissues were homogenized and incubated with ONOO$^-$ to activate Pro-MB. The percentage injected dose (ID%) of SCAN in tumour was calculated to be 3.9 ± 0.7%, which was lower than that in liver (4.9 ± 0.7%) yet higher than that in spleen (3.2 ± 0.8%) and lung (2.1 ± 0.4%) (Supplementary

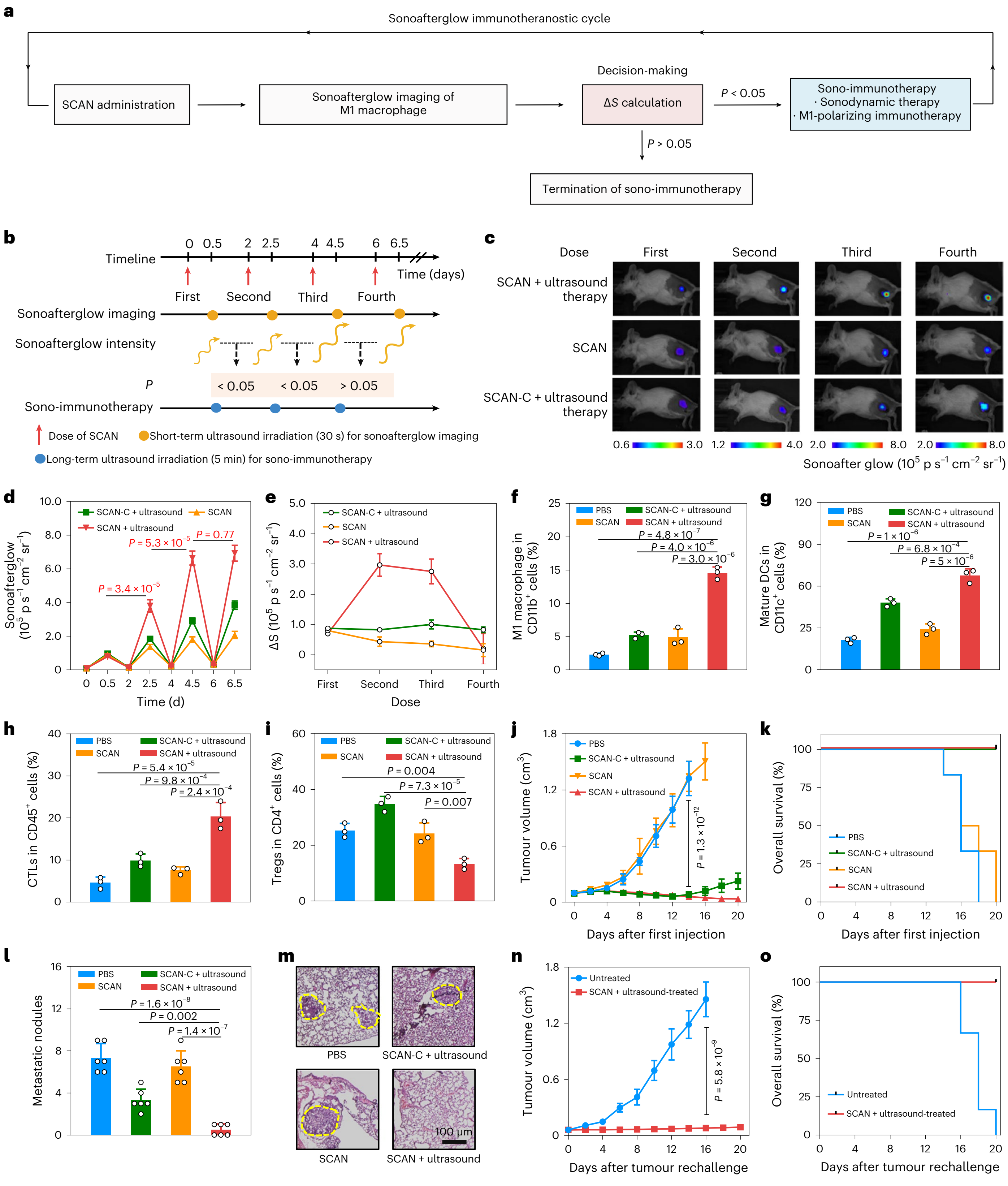

Fig. 37). However, Pro-R837 was barely activated in those main organs (Supplementary Fig. 38), which was benefited from dual-lock design of SCAN. In addition, all the components of SCAN are biologically benign organic molecules that could be cleared by the liver or kidney[38–41]. This was supported by the data showing no weight loss or abnormal serological and histological indicators of mice after treatment (Supplementary Fig. 39).

Discussion

To circumvent the limited tissue depth of signal induction needed for photo-induced afterglow, we invented ultrasound-induced afterglow nanoparticles (SNAPs) with tuneable emissions from the visible to the NIR range (780 nm) and a long half-life (up to 180 s) (Fig. 1). Mechanistically, sonoafterglow resembled photoafterglow, both of which were initiated by an $^1O_2$-generating sensitizer to generate a long-lasting luminescent intermediate. However, the sonoafterglow of NCBS/DPAs SNAP was 2.4 times brighter than its photoafterglow (application for 30 s), because the sonodynamic process had higher efficacy of $^1O_2$ production than the photodynamic process. The more $^1O_2$ generation under ultrasound application might be caused by the unique sonophysicochemical processes (that is, the sonoluminescence, pyrolytic reactions and acoustic cavitation effects) that facilitate energy transfer from the sensitizer to surrounding oxygen molecules[42,43], which were not present under light irradiation. Note that sonolysis, a process of ultrasound-induced ·OH production, was negligible in this study possibly owing to the low pulse-repetition frequency (100 Hz) and sonosensitizer types[44,45]. In addition to $^1O_2$ generation triggered by the initiator, sonoafterglow was dependent on the chemiluminescence quantum yield of the substrate, the energy transfer to the initiator and the fluorescence quantum yield of the initiator. These factors were varied in different SNAPs; thus, the $^1O_2$ generation efficiencies (Fig. 2c and Supplementary Fig. 1) were not fully consistent with the sonoafterglow signals (Figs. 1d). More importantly, ultrasound enabled signal induction for NCBS/DPAs SNAP seated deeply in tissue of 4 cm thickness (Fig. 2), which was twice as deep as its photoafterglow. As a result of high brightness and deep-tissue imaging, subcutaneously implanted NCBS/DPAs SNAP showed nearly ten-fold higher in vivo afterglow signal (2.3×10^5 (p s^{-1} cm^{-2} sr^{-1})/(μg ml^{-1})) than the reported subcutaneously implanted X-ray-induced afterglow nanoparticles based on the same mass dosage (2.5×10^4 (p s^{-1} cm^{-2} sr^{-1})/(μg ml^{-1}) for $LiGa_5O_8$:Cr NPs). Moreover, NCBS/AMPA SNAP was brighter than all existing organic photoafterglow nanoparticles and at least 190 times higher than inorganic photoafterglow nanoparticles (Supplementary Table 2). Thus, SNAPs set a record in both tissue depth and brightness for afterglow imaging.

The modular composition of SNAPs allowed their development into activatable probes that turned on sonoafterglow only in the presence of cancer biomarkers. This may not be easily feasible for X-ray-induced afterglow in inorganic nanoparticles[19]. As the $^1O_2$-generating initiator and the sonoafterglow substrate are two essential components for sonoafterglow emission, either the initiator or the substrate could be molecularly silenced and designed to be activated by targeted biomarkers. To detect ONOO$^-$, a biomarker produced mainly by M1 macrophages that characterizes a pro-inflammatory tumour microenvironment, SNAP-M and SCAN were designed to, respectively, have a silenced sonoafterglow substrate (Pro-DPAs) or initiator (Pro-MB), both of which functioned to specifically turn on their sonoafterglow in the presence of ONOO$^-$. Such a biomarker-activated sonoafterglow in SNAPs eliminated the non-specific signal from passively accumulated probes, permitting the direct correlation of sonoafterglow with the level of intra-tumoural M1 macrophages and thus the precise monitoring of pro-inflammatory tumour microenvironment during cancer immunotherapy. Owing to deep-tissue imaging and minimal background noise, the activatable sonoafterglow nanoprobe (SNAP-M) afforded an SBR of 72.2 for in vivo imaging of ONOO$^-$ in the tumour of living mice, which was 2.5 times higher than its photoafterglow (28.9) and even substantially higher than biomarker-activatable photoacoustic probes and second NIR fluorescent probes used in vivo (SBR <20) (Supplementary Table 3). We validated SNAP-M for the deep-tissue (at least 2 cm) evaluation of M1 macrophages during immunotherapy. It had an accuracy level similar to that of invasive flow-cytometry analysis of tumour tissues (Fig. 3). We also tested SCAN in mice with deep-seated peritoneal 4T1 tumours, wherein the sonoafterglow clearly identified the tumour nodules. Its SBR was 6.0 times higher than fluorescence (Supplementary Fig. 40). Thus, SNAPs represent a new class of smart probes for the non-invasive screening of immunotherapeutic agents in living animals.

Taking advantage of the remote ultrasound-charging process, we further used SNAP as a cancer immunotheranostic agent (SCAN) by doping them with a silenced immune prodrug (Pro-R837). SCAN required both ultrasound and ONOO$^-$ in the pro-inflammatory tumour microenvironment to activate its immunotheranostic function (Fig. 4). This dual-lock design is distinct from that of existing nanoimmunotheranostic agents with 'always-on' signals and pharmaceutical effects[46–49] that are non-specifically released in normal tissues and thus can cause side effects. In addition to the advantage of remotely controlled immunotherapeutic activation specifically in the tumour, SCAN emitted ONOO$^-$-correlated sonoafterglow to report the levels of M1 macrophages in the pro-inflammatory tumour microenvironment in real time, revealing that exact four-dose treatments were sufficient for the full polarization of the intra-tumoural macrophages (Fig. 5). Notably, the total dose of R837 administered to mice was at least three times lower than other reported Toll-like-receptor-agonist-loaded nanoparticles for the M1-oriented macrophage polarization in tumours[50,51]. With such a sonoafterglow-guided immunotherapeutic regimen, SCAN precisely elicited effective anti-tumour immunity at the right dosage, leading to complete tumour suppression and metastasis inhibition. Thus, SCAN can be used to guide cancer immunotherapy and for the remote control of immunotherapeutic action.

In summary, we have reported a library of ultrasound-induced afterglow nanoparticles (SNAPs) for deep-tissue-inducible and background-free optical imaging in living animals. By virtue of the modular sonoafterglow mechanism, SNAPs can be developed into activatable theranostic nanoprobes for the accurate detection of subtle molecular changes in diseased microenvironments and to longitudinally monitor therapeutic outcomes to guide an intervention. In addition to its potential for in vivo drug screening and precision medicine, the tissue depth of sonoafterglow imaging may provide opportunities for the real-time non-invasive detection of physiopathological processes at sensitivity levels and tissue depths not achievable by other optical modalities.

Methods

Synthesis of Pro-R837

To synthesize Linker 1, trifluoroacetic acid (415 μl, 5.43 mmol) was added dropwise to the mixture of mercaptoacetic acid (10 g, 108.6 mmol) and dry acetone (4.02 ml, 54.3 mmol) over 10 min. Then, the reaction was stirred for 6 h until the mixture had a large amount of white precipitate. The white solid was washed by diethyl ether (30 ml) three times to give pure product Linker 1 (23.4 g, 96%). ^{1}H NMR ($CDCl_3$, 400 MHz): δ 3.53 (s, 4H), 1.63 (s, 6H). ^{13}C NMR (100 MHz, $CDCl_3$): δ 177.2, 56.5, 33.3, 29.9. HRMS (ESI) *m*/*z*: [M − H]$^-$ calc. for $C_7H_{11}O_4S_2$ 223.0099; found 223.0098. To synthesize Linker 2, the mixture of $NaBH_4$ (5.0 g, 132.3 mmol) and Linker 1 (5.0 g, 22.2 mmol) were added to dry tetrahydrofuran (THF, 100 ml) at 0 °C. Subsequently, iodine (20 g, 78.8 mmol) in dry THF (100 ml) was added dropwise by a funnel for 0.5 h at 0 °C. Then, the mixture was heated to reflux for 20 h and cooled to room temperature. Next, CH_3OH (50 ml) was slowly added until the reaction became clear. The mixture was concentrated under vacuum and purified by silica gel column chromatography using CH_2Cl_2/ethyl acetate (1/1, v/v) as eluent to give the colourless oil (2.48 g, 57%). ^{1}H NMR ($CDCl_3$, 400 MHz): δ 3.80 (t, *J* = 6.2 Hz, 4H), 2.89 (t, *J* = 6.0 Hz, 4H), 1.64 (s, 6H). ^{13}C NMR (100 MHz, $CDCl_3$): δ 61.4, 56.0, 33.7, 31.3. HRMS (ESI) *m/z*: [M + H] $^+$ calc. for $C_7H_{17}O_2S_2$ 197.0670; found 197.0684. To synthesize Pro-R837, triphosgene (712.2 mg, 2.4 mmol) in dry THF (3 ml) was dropwise added to the mixture of R837 (192.2 mg, 0.8 mmol) and 4-dimethylaminopyridine (DMAP) (293.2 mg, 2.4 mmol) in 10 ml of THF at 0 °C under N_2 atmosphere. Then, triethylamine (Et_3N) (669 µl, 4.8 mmol) was added into the reaction, and the mixture was stirred for 2 h. The residue was afforded after solvent was removed by vacuum and the excessive triphosgene was blown away via N_2. Subsequently, Linker 2 (470.5 mg, 2.4 mmol) and Et_3N (669 µl, 4.8 mmol) in dry THF (10 ml) were added quickly into the residue at 0 °C. Next, the mixture was stirred for 36 h at room temperature, which was further purified by HPLC using CH_3OH/H_2O as eluent to give white solid Pro-R837 (36.2 mg, 9.8%). ^{1}H NMR ($CDCl_3$, 400 MHz): δ 8.32 (s, 1H), 8.14–8.18 (m, 2H), 7.87 (t, *J* = 7.2 Hz, 1H), 7.79 (t, *J* = 7.2 Hz, 1H), 4.53 (t, *J* = 13.5 Hz, 2H), 4.47 (d, *J* = 4.8 Hz, 2H), 3.93 (m, 2H), 3.06 (t, *J* = 7.2 Hz, 1H), 2.93 (m, 2H), 2.31 (m, 1H), 1.61 (s, 6H), 1.06 (d, *J* = 4.8 Hz, 6H). MS (ES+): *m/z* calc. for $C_{22}H_{31}N_4O_3S_2$ 463.18; found: 462.96 $[M + H]^+$.

Synthesis of Pro-MB

Toluene (40 ml), sodium bicarbonate (294 mg, 3.5 mmol) and sodium dithionate (522.3 mg, 3 mmol) were sequentially added to the solution of MB (373.9 mg, 1 mmol) in water (10 ml), which was stirring at 50 °C for 30 min. When the mixture turned pale yellow, the toluene phase containing leuco-MB was separated and dried by anhydrous Na_2SO_4 and transferred to solvent of Vilsmeier–Haack reagent in dry THF (10 ml). The residue was washed by saturated NaCl solution (50 ml) and ethyl acetate (40 ml) three times. The organic layer was dried by anhydrous Na_2SO_4 and concentrated under vacuum. The white solid Pro-MB (42% yield) was afforded by silica gel column chromatography using CH_2Cl_2/ethyl acetate (1/1, v/v) as eluent. ^{1}H NMR ($CDCl_3$, 400 MHz): δ 8.55 (s, 1H), 7.56 (dd, J_1 = 6.8 Hz, 1H), 6.64–6.91 (m, 4H), 6.59 (dd, J_2 = 3.2 Hz, 1H), 2.94 (d, *J* = 4.8 Hz, 12H). ^{13}C NMR (100 MHz, $CDCl_3$): δ 161.2, 149.4, 149.3, 131.8, 130.3, 127.3, 125.7, 125.2, 122.4, 111.1, 111.0, 110.7, 110.3, 40.7. HRMS (ESI) *m/z*: [M + H] + calc. for $C_{17}H_{20}N_3OS$ 314.1327; found 314.1323. Vilsmeier–Haack reagent was prepared as follows: thionyl chloride ($SOCl_2$, 183 µl, 2.5 mmol) dissolved in 5 ml dichloromethane was added dropwise to a solution of dry dimethylformamide (DMF) (100 µl) in DCM (10 ml) at room temperature under N_2 atmosphere. Then, the mixture was stirred at 60 °C for 15 min and evaporated on a rotary evaporator to afford the Vilsmeier–Haack reagent.

Synthesis of AMPA

Compound 2-azidoethan-1-amine[39] (64.5 mg, 0.75 mmol), N-ethoxycarbonyl-2-ethoxy-1,2-dihydroquinoline (EEDQ) (185 mg, 0.75 mmol) and compound 2-azidoethan-1-amine (MPA) (102.1 mg, 0.3 mmol) were added in THF (20 ml) under N_2 atmosphere. The reaction was stirred and monitored by HPLC. After completion, the reaction mixture was concentrated by evaporation, and crude product was purified by HPLC using CH_3OH/H_2O as eluent to afford AMPA (113.8 mg, 93%) as a white solid. ^{1}H NMR ($CDCl_3$, 400 MHz): δ 7.96 (d, *J* = 12 Hz, 1H), 7.40 (d, *J* = 8.4 Hz, 1H), 6.85 (s, 2H), 6.59 (d, *J* = 16.4 Hz, 1H), 6.01 (t, *J* = 5.2 Hz, 1H), 3.54–3.61 (m, 4H), 3.31 (s, 3H), 3.23 (s, 1H), 2.7 (s, 1H), 2.75–1.92 (m, 12H). ^{13}C NMR (100 MHz, $CDCl_3$): δ 167.9, 155.9, 142.9, 138.6, 137.7, 133.4, 128.7, 121.6, 121.1, 120.1, 117.2, 58.1, 51.1, 39.3, 39.2, 37.2, 32.5, 30.5, 28.4. HRMS (ESI) *m/z*: $[M + H]^+$ calc. for $C_{23}H_{29}N_4O_3$ 409.2240; found 409.2234.

Preparation of SNAPs and SNAP-M

Sonoafterglow components including RB, PA[52], DPA_X (*X* = O and S) and Pro-DPAs were synthesized according to the literature[29]. MEHPPV, VP, NCBS and MB were purchased from Sigma-Aldrich. HMP was obtained from MedChemExpress. Sonoafterglow initiators (including RB, HMP, VP and NCBS) and substrates (including AMPA, PA, MEHPPV, DPAo and DPAs) were, respectively, dissolved in THF (or other appropriate solvents, for example, CH_3OH) to obtain the stock solution (1 mg ml^{-1}). PEG-*b*-PPG-*b*-PEG (Sigma-Aldrich) was dissolved in THF to obtain the stock solution (20 mg ml^{-1}). The initiator (4 µl), substrate (20 µl) and PEG-*b*-PPG-*b*-PEG (20 µl) were mixed in a 10 ml glass bottle under vortex, followed by rotary evaporation to remove THF and afford a thin film on inner wall. The obtained film was hydrated in 1 ml of distilled de-ionized water or PBS under vigorous vortex to obtain SNAP solution. The solution was filtrated through 0.22 µm sterilizing-grade membranes and concentrated by ultracentrifugation. The solution was freeze-dried to obtain SNAP powder. SNAP powder was dissolved in THF, and the concentration of each component was determined using UV–vis spectrometer. The encapsulation efficiency (EE%) was calculated by encapsulated drug divided by the total drug added. For instance, the EE% was, respectively, calculated to be 96.1 ± 2.6% and 96.4 ± 2.4% for NCBS and DPAs in SNAP. SNAP-M was prepared accordingly using Pro-DPAs (20 µl, 1 mg ml^{-1}), NCBS (4 µl, 1 mg ml^{-1}) and PEG-*b*-PPG-*b*-PEG (20 µl, 20 mg ml^{-1}).

Preparation of SCAN

Sonoafterglow initiators (Pro-MB), substrates (including AMPA, PA, MEHPPV, DPAo, DPAs) and Pro-R837 were, respectively, dissolved in THF to obtain stock solutions. Pro-MB (4 µl, 1 mg ml^{-1}), AMPA (20 µl, 1 mg ml^{-1}), Pro-R837 (8 µl, 1 mg ml^{-1}) and PEG-*b*-PPG-*b*-PEG (20 µl, 20 mg ml^{-1}) were mixed in 10 ml glass bottle using vortex. THF removal, hydration, filtration and ultracentrifugation were conducted as stated. The solution was freeze-dried to obtain SCAN powder. SNAP powder was dissolved in THF and the concentration of each component was determined using UV–vis spectrometer or HPLC (methanol:water at 70–95% gradient, 0.1% trifluoroacetic acid). The EE% was calculated as previously stated and to be 97.2 ± 1.9% for Pro-MB, 98.0 ± 2.6% for AMPA and 97.0 ± 1.4% for Pro-R837 in SCAN.

Cell culture and animal models

NIH 3T3 murine embryonic fibroblast cells (CRL-1658), 4T1 murine breast cancer cells (CRL-2539) and Raw 264.7 murine macrophages (TIB-71) were purchased from American Type Culture Collection. Balb/c mice and nude mice were purchased from InVivos. Cells were maintained in Dulbecco's modified Eagle medium (DMEM) or Roswell Park Memorial Institute Medium (RPMI1640) containing 10% foetal bovine serum in a humidified environment containing 5% CO_2 and 95% air at 37 °C. All animal experiments were carried out in accordance with Guidelines for Care and Use of Laboratory Animals of the NTU Institutional Animal Care and Use Committee (IACUC) and approved by the IACUC for Animal Experiment, Singapore. Mice were group-housed in ventilated clear plastic cages under appropriate ambient temperature (~22 °C), humidity (50%) and standard 12 h:12 h light:dark conditions. To establish 4T1 breast cancer model, 2×10^6 4T1 cancer cells suspended in 0.2 ml DMEM were subcutaneously injected to the right flank of Balb/c mice (female, 5–6 weeks). Tumour size was calculated as $V = ab^2/2$, where *a* represents tumour length and *b* represents tumour width. Treatments were initiated when tumour size reached 100 mm^3 unless otherwise stated. Mice were killed when tumour length exceeded 1.5 cm in diameter. Mice were weighed every other day during treatment.

Instrument settings

The absorbance and fluorescence spectra of sonoafterglow initiators and substrates dissolved in appropriate organic solvent were recorded using UV spectrometer and fluorometer (Horiba), respectively. The absorbance and emission intensity were normalized. ^{1}H NMR spectra were obtained using AVIII 400 MHz NMR (Bruker) and analyzed by Mestre Nova LITE v5.2.5–4119 software (Mestrelab Research). The hydrodynamic size of nanoparticle was measured using Nano-ZS Particle Sizer (Malvern). The morphology of nanoparticle was studied using JEM 1400 TEM (JEOL). NIR fluorescence images of nanoparticle solution in thin-wall tube were acquired by IVIS Spectrum CT In Vivo Imaging System (IVIS, PerkinElmer) under fluorescence mode. Sonoafterglow was induced by ultrasound generated from Intelect Mobile Ultrasound device (1.0 MHz, 0–2.5 W cm^{-2}, 50% duty cycle, 100 Hz, from Chattanooga). Photoafterglow was induced by 808 nm high-power NIR laser (operating mode: continuous wave, output power after fibre: 2.5 W, from CNI) or 680 nm high-power laser (operating mode: continuous wave, output power after fibre: 0.5 W, from CNI). HPLC analysis and purification were performed on an Agilent 1260 system using CH_3OH/H_2O as the eluent. Sonoafterglow (or photoafterglow) was detected using IVIS under bioluminescence mode with open filter (for optical intensity determination) or with specific emission filters (for spectrum recording) after cessation of ultrasound (or laser) application (within 5 s).

Characterization

Both fluorescence and afterglow images were quantified by region of interest analysis using Living Imaging 4.3 Software. To study the sonoafterglow half-life, SNAPs were ultrasound irradiated (2.0 W cm^{-2}) for 30 s, followed by detection using IVIS under IVIS bioluminescence mode with open filter at continuous timepoints. The sonoafterglow lifetime of nanoparticle was obtained by plotting sonoafterglow intensity as a function of time. $^1O_2$ generation upon ultrasound or laser irradiation was measured by fluorescence enhancement of singlet oxygen sensor green (SOSG, Thermo Fisher Scientific) recorded by fluorometer according to manufacturers' instructions. To quantify the reactive oxygen species generation, 100 µL of NCBS SNAP solutions (0.1 ml, 20 µg ml^{-1}, in 1× PBS) were mixed with 10 µl of $^1O_2$ trapping agent 2,2,6,6-tetramethylpiperidine (TEMP, Dojindo Molecular Technologies) or ·OH and $O_2^{\bullet-}$ trapping agent 5,5-dimethyl-1-pyrroline *N*-oxide (DMPO, Dojindo Molecular Technologies), followed by ultrasound application (1.0 MHz, 2.0 W cm^{-2}, 50% duty cycle) for 30 s. Immediately after treatment, ESR spectra of the samples were recorded using ESR spectroscopy. The generation of $^1O_2$ was quantified by measuring the amounts of free electrons and normalized to the mass of samples. To study whether sonoafterglow can be repeatedly induced, NCBS/DPAs SNAP solution (in PBS, pH 7.4, 0.01 M) was irradiated by ultrasound application for five cycles and sonoafterglow signals were detected after each cycle. Accordingly, sonoafterglow signals were also detected from NCBS/DPAs SNAP in other biological buffers including Tris (0.01 M), HEPES (0.01 M) and DMEM culture medium.

In vitro tissue penetration assays

NCBS/DPAs SNAP ([DPAs] = 100 µg ml^{-1}) was placed under chicken breast tissue with different thickness. NIR fluorescence was captured through chicken breast (excitation wavelength 710 nm, detection wavelength 780 nm, acquisition time 0.1 s). Sonoafterglow and photoafterglow were, respectively, induced through chicken breast by ultrasound application (2.0 W cm^{-2}) for 30 s and laser irradiation (808 nm, 0.33 W cm^{-2}) for 90 s and detected through chicken breast under IVIS bioluminescence mode with open filter (acquisition time 1 s) after cessation of irradiation. For further comparison, sonoafterglow and photoafterglow were induced without chicken breast yet detected through chicken breast with different thickness. NCBS/DPAs SNAP solution was also placed under a living mouse (tissue depth 1.8 cm) for signal induction and detection under the above settings.

Cell viability assay

To compare the cell viability during sonoafterglow imaging, M0 macrophages were seeded in 96-well plates at a density of 5 × 10^3 cells per well. After 24 h incubation, the medium was replaced by fresh medium containing NCBS/DPAs SNAP ([DPAs] = 4, 20 or 100 µg ml^{-1}) for further incubation. After 12 h, the medium was refreshed, and cells were ultrasound-irradiated (2.0 W cm^{-2}) or photo-irradiated (808 nm, 0.33 W cm^{-2}) for 30 s and incubated for further 24 h. 3-(4,5-dimethylthiazol-2-yl)-5-(3-carboxymethoxyphenyl)-2-(4-sulfophenyl)-2H-tetrazolium (MTS) reagent was then added into medium in 1-to-10 volume ratios for cell incubation. After incubation for 3 h, the absorbance at 490 nm for each well was measured using microplate reader (SpectraMax). To study the cell viability under different ultrasound application time, 4T1 cancer cells were seeded in 96-well plates at a density of 5 × 10^3 cells per well. After 24 h incubation, the medium was replaced by fresh medium containing NCBS/DPAs SNAP ([DPAs] = 20 µg ml^{-1}) for further incubation. After 12 h, the medium was refreshed, and cells were ultrasound-irradiated (2.0 W cm^{-2}) or photo-irradiated (808 nm, 0.33 W cm^{-2}) over time (up to 5 min) and incubated for further 24 h. MTS agent was applied for cell viability determination as described. Accordingly, 4T1 cancer cells (5 × 10^3 cells per well) were incubated with SCAN ([Pro-MB] = 30 µM) pre-treated with or without ONOO$^-$. After 12 h, the medium was refreshed and cells were ultrasound-irradiated over time (up to 5 min) and cell viability was determined using MTS agent as stated. To study whether the cell viability was contributed by cavitation effect of ultrasound application, 4T1 cancer cells in 96-well plates (5 × 10^3 cells per well) were incubated with SNAPc (SNAP without NCBS). After 12 h incubation, the medium was refreshed, and cells were ultrasound-irradiated (2.0 W cm^{-2}) for 5 min. MTS agent was applied for cell viability determination as described.

In vitro macrophage polarization

M0 macrophages (Raw 264.7) were seeded on six-well plate (5 × 10^5 cells per well). After incubation for 12 h, cells were incubated with lipopolysaccharides (100 ng ml^{-1}, Sigma-Aldrich) and IFN-γ (50 ng ml^{-1}, BioLegend) for M1 macrophage polarization, or IL-4 (10 ng ml^{-1}, BioLegend) for M2 macrophage polarization[31]. After incubation for 2 days, macrophages were blocked with antibodies against CD16/32 (93, 1:50, BioLegend), then stained with live/dead staining kit (L23105, Thermo Fisher Scientific), antibody against F4/80 (BM8, 1:20, BioLegend) and antibody against iNOS (W16030C, 1:160, BioLegend), followed by analysis using LSR Fortessa flow cytometer (BD Biosciences). Data were analyzed using FlowJo v10 software.

ONOO$^-$ responsiveness of SNAP-M and SCAN

SNAP-M ([Pro-DPAs] = 40 µM) or SCAN ([Pro-MB] = 30 µM) was incubated with different RONS (80 µM for SNAP-M and 60 µM for SCAN) or metal ions (100 µM) at 37 °C for 10 min followed by sonoafterglow imaging using IVIS under bioluminescence mode with open filter (acquisition time 1 s). The stock solutions of different RONS were prepared according to literature[29]. Briefly, $O_2^{\bullet-}$ was provided by KO_2 in DMSO; hydroxyl radical (•OH) was obtained by Fenton reaction between H_2O_2 and $FeSO_4{\bullet}7H_2O$; $^1O_2$ was produced by adding NaOCl to H_2O_2; commercially available sodium peroxynitrite (source of ONOO$^-$), NaOCl (source of ClO$^-$) and H_2O_2 solutions were used without further purification. The LOD was calculated by the fitting curve of sonoafterglow intensity as a function of ONOO$^-$ concentration, which was based on 3σ/slope, where σ is the standard deviation (s.d.) of the blank samples. To study the dual-locked activation of Pro-R837, SCAN ([Pro-MB] = 30 µM) was incubated with or without ONOO– (60 µM), followed by ultrasound application. The resultant solutions were analyzed using HPLC. Free R837 and MB were used for reference. The kinetics of Pro-R837 activation was determined using HPLC and plotted as a function of ultrasound application time.

Specific detection of M1 macrophages by SNAP-M and SCAN

M0, M1 and M2 macrophages, 4T1 cancer cells and NIH 3T3 cells were, respectively, seeded in glass-bottom dish (1 × 10^5 per well) and incubated with SNAP-M ([Pro-DPAs] = 20 µg ml^{-1}) or SCAN ([AMPA] = 50 µg ml^{-1}) for 12 h. To scavenge ONOO$^-$, M1 macrophages were pre-treated with *N*-acetylcysteine (100 mM) for 2 h. Cells were washed thrice with PBS and stained with NucBlue (R37605, Invitrogen) for 15 min, followed by fluorescence imaging using LSM800 confocal laser scanning microscope (Carl Zeiss). Sonoafterglow was induced by ultrasound application (2.0 W cm^{-2}) for 30 s and detected immediately by LX71 inverted microscope (Olympus) equipped with CCD camera with the excitation light blocked. Quantification of signal intensity was conducted using Image J v1.51a software.

In vitro theranostics by SCAN

M2 macrophages were seeded on six-well plate (5×10^5 cells per well). After incubation for 12 h, they were treated with PBS (negative control), non-activated SCAN (ultrasound-irradiated only, [Pro-R837] = 10 μg ml^{-1}), fully activated SCAN (ultrasound-irradiated and ONOO$^-$-treated) or R837 (5.1 μg ml^{-1}, positive control) for 2 days. For washout, cells were incubated with fresh culture medium for another day. Next, all cells were incubated with intact SCAN ([Pro-MB] = 30 μM) for 2 h. Cells were washed thrice with PBS, and then ultrasound pre-irradiated (2.0 W cm^{-2}) for 30 s. Sonoafterglow images were captured immediately by LX71 inverted microscope (Olympus) equipped with CCD camera with the excitation light blocked. Quantification of signal intensity was conducted using Image J v1.51a software.

Biodistribution of SNAP-M and SCAN

4T1 tumour-bearing mice ($n = 3$ per group) were intravenously injected with SNAP-M ([Pro-DPAs] = 250 μg ml^{-1}, 200 μl), followed by in vivo NIR fluorescence imaging at pre-determined timepoint (0, 12, 24, 36 and 48 h) using IVIS (acquisition time 0.1 s, excitation wavelength 710 nm, detection wavelength 780 nm). Mice were killed at 48 h after injection, and tumours and organs (heart, liver, spleen, lung and kidneys) were collected for ex vivo NIR fluorescence imaging using IVIS (acquisition time 0.1 s, excitation wavelength 710 nm, detection wavelength 780 nm). 4T1 tumour-bearing mice ($n = 3$ per group) were intravenously injected with SCAN ([AMPA] = 250 μg ml^{-1}, 200 μl), followed by in vivo NIR fluorescence imaging at pre-determined timepoint (0, 2, 4, 6, 12, 24 and 36 h) using IVIS (acquisition time 0.1 s, excitation wavelength 660 nm, detection wavelength 700 nm). Mice were killed at 12 h after injection, and tumours and organs were collected for ex vivo NIR fluorescence imaging using IVIS (acquisition time 0.1 s, excitation wavelength 660 nm, detection wavelength 700 nm). To fully activate Pro-MB for fluorescence imaging, tumours and organs were homogenized and incubated with ONOO$^-$ (0.1 mM) for 2 h. The percentage injected dose (ID%) of SCAN was calculated by dividing the content of Pro-MB in organs by the total injected Pro-MB of SCAN. To study the SCAN uptake by macrophages and cancer cells, 4T1 tumour homogenates from mice intravenously injected with SCAN were processed to be single-cell suspension, which were stained with antibodies against F4/80 (BM8, 1:20) and CD45 (30-F11, BioLegend) for flow-cytometry analysis. The percentage of MB$^+$ macrophages (CD45$^+$F4/80$^+$) and cancer cells (CD45$^-$) was calculated.

In vivo sonoafterglow imaging by SNAP-M

4T1 tumour-bearing mice ($n = 3$ per group) were intraperitoneally injected with R848 (0.4 mg ml^{-1}, 50 μl) or saline every other day three times. At day 6, SNAP-M ([Pro-DPAs] = 50 μg ml^{-1}, 50 μl) was intra-tumourally injected at 2 h before imaging. Fluorescence images were captured with 0.1 s of acquisition time (excitation wavelength 710 nm, detection wavelength 780 nm). For sono- and photoafterglow imaging, tumours were pre-irradiated with ultrasound (2.0 W cm^{-2}) or laser (808 nm, 0.33 W cm^{-2}) for 30 s, and afterglow signals were detected using IVIS (acquisition time 10 s). To study the tissue penetration of sonoafterglow imaging by SNAP-M, tumours were covered with chicken breast of different thickness (0, 0.5, 1, 2 and 3 cm). Fluorescence images were captured through tissues with 0.1 s of acquisition time (excitation wavelength 710 nm, detection wavelength 780 nm). Sonoafterglow or photoafterglow were induced through tissues by ultrasound (2.0 W cm^{-2}) for 30 s or laser (808 nm, 0.33 W cm^{-2}) for 90 s and detected through tissues using IVIS (acquisition time 10 s).

In vivo sonoafterglow theranostic property of SCAN

4T1 tumour-bearing mice ($n = 3$ per group) were intraperitoneally injected with R837 (0.4 mg ml^{-1}, 50 μl) or saline every other day three times. At day 6, SCAN ([AMPA] = 50 μg ml^{-1}, 50 μl) was intra-tumourally injected at 2 h before imaging. Fluorescence images were captured with 0.1 s of acquisition time (excitation wavelength 660 nm, detection wavelength 700 nm). For sono- and photoafterglow imaging, tumours were pre-irradiated with ultrasound (2.0 W cm^{-2}) or laser (680 nm, 2.0 W cm^{-2}, maximum permissive exposure) for 30 s, and afterglow signals were detected using IVIS (acquisition time 10 s). To study the afterglow imaging after intravenous injection of SCAN, 4T1 tumour-bearing mice were randomly divided into four groups ($n = 6$ per group): (1) PBS, (2) SCAN-C (without Pro-R837, [AMPA] = 250 μg ml^{-1}, 200 μl) plus long-term ultrasound application (2.0 W cm^{-2}, 5 min) (SCAN-C + ultrasound therapy), (3) SCAN ([AMPA] = 250 μg ml^{-1}, 200 μl), (4) SCAN plus long-term ultrasound application (SCAN + ultrasound therapy). Long-term ultrasound application was conducted on tumours to perform sono-immunotherapy. On day 0, SCAN-C or SCAN was intravenously administered. After 12 h, sonoafterglow imaging was conducted, and long-term ultrasound application was executed on tumours. On day 2, a fresh dose of SCAN-C or SCAN was injected, and the procedures above were repeated. Such a therapeutic regimen was discontinued until the fourth cycle. To study the immunological memory, SCAN + ultrasound therapy-treated and untreated mice ($n = 6$ per group) were challenged by subcutaneous inoculation of 4T1 cancer cells (2×10^6 cells in 100 μl DMEM). Tumour size was recorded every 2 days. Mice were killed within 3 weeks after inoculation.

Flow-cytometry analysis

Tumours were dissected and digested with collagen I (2 mg ml^{-1}), collagen IV (2 mg ml^{-1}) and DNase I (0.2 mg ml^{-1}) prepared in DMEM culture medium in 37 °C water bath. Digested tissues were then incubated with red blood cell lysis buffer (420301, BioLegend) for 5 min, followed by passing through a 100 μm mesh strainer (352360, Falcon). The obtained single-cell suspensions were incubated with dye-conjugated antibodies according to the manufacturer's instructions. Live/dead staining kit (L23105, Thermo Fisher Scientific) was used to identify the living cells. All antibodies were purchased from BioLegend unless otherwise indicated. Antibody against CD16/32 (93, 1:50) was used to block the non-specific binding. Antibodies against CD11b (M1/70, 1:200), F4/80 (BM8, 1:20) and iNOS (W16030C, 1:160) were used for M1 macrophage staining. Antibodies against CD45 (30-F11, 1:200), CD3 (17A2, 1:100) and CD8 (53–6.7, 1:100) were used for CTL staining. Antibodies against CD4 (RM4–5, 1:100) and FOXP3 (MF-14, 1:200) were used for T_{Reg} cell staining. Antibodies against CD62L (MEL-14, 1:100) and CD44 (IM7, 1:20) were used for memory T-cell staining. Antibodies against CD11c (N418, 1:100), CD80 (16-10A1, 1:50) and CD86 (A17199A, 1:50) were used for mature DC staining. Cells were then analyzed with an LSR Fortessa flow cytometer (BD Biosciences). Data were analyzed using FlowJo v10 software.

Histological analysis

Metastatic nodules on lungs were counted. Tumours and main organs (including heart, liver, spleen, lung, kidney and skin) were collected, treated with 4% paraformaldehyde for 24 h and 30% sucrose for another 48 h, followed by cryo-sectioning using CryoStat CM1950 (Leica). Tumour slices were stained with antibodies against HMGB-1 (3E3, Alexa Fluor 488-labelled, 1:200, BioLegend), Caspase-3 (#9664, rabbit anti-mouse, 1:400, Cell Signalling Technology) and rabbit anti-mouse calreticulin (PA3-900, 1:200, Thermo Fisher Scientific). Alexa Fluor 488-conjugated secondary antibody (goat anti-rabbit, 1:500, Thermo Fisher Scientific) was used in caspase-3 and calreticulin staining. Immunofluorescence was observed using LSM800 confocal microscope (Carl Zeiss). Moreover, tumour and organs sections were subjected to haematoxylin and eosin (H&E) staining and observed using LX71 inverted microscope (Olympus).

Cytokines and biochemical indexes determination

To detect intra-tumoural immune cytokines, tumours were extracted from mice on day 8 and homogenized. The supernatant was collected through centrifugation (500*g*, 5 min). Intra-tumoural cytokines, including IFN-γ, IL-12, IL-10 and TGF-β, in the supernatant were determined using ELISA kits (BioLegend) according to the manufacturer's instructions. On day 8, sera were collected from mice and blood urea nitrogen, creatinine, aspartate aminotransferase and alanine aminotransferase were determined according to the instructions of the manufacturer (Sigma-Aldrich).

Statistical analysis

All numeric data are presented as mean ± s.d. unless otherwise indicated. The significance between two groups was analyzed by two-tailed Student's *t*-test. The significance between multiple groups was analyzed by one-way analysis of variance (ANOVA) with Tukey's post hoc test. Statistical analysis was performed using GraphPad Prism 7.0. P values less than 0.05 were considered significant. $^*P < 0.05$, $^{**}P < 0.01$, $^{***}P < 0.001$.

Reporting summary

Further information on research design is available in the Nature Portfolio Reporting Summary linked to this article.

Data availability

The main data supporting the results in this study are available within the paper and its Supplementary Information. The raw and analyzed datasets generated during the study are too large to be publicly shared, yet they are available for research purposes from the corresponding author on reasonable request. Source data are provided with this paper.

References

1. Michalet, X. et al. Quantum dots for live cells, in vivo imaging, and diagnostics. *Science* **307**, 538–544 (2005).
2. Gao, X., Cui, Y., Levenson, R. M., Chung, L. W. & Nie, S. In vivo cancer targeting and imaging with semiconductor quantum dots. *Nat. Biotechnol.* **22**, 969–976 (2004).
3. Hong, G., Antaris, A. L. & Dai, H. Near-infrared fluorophores for biomedical imaging. *Nat. Biomed. Eng.* **1**, 0010 (2017).
4. Chang, B. et al. A phosphorescent probe for in vivo imaging in the second near-infrared window. *Nat. Biomed. Eng.* **6**, 629–639 (2022).
5. Miao, Q. et al. Molecular afterglow imaging with bright, biodegradable polymer nanoparticles. *Nat. Biotechnol.* **35**, 1102–1110 (2017).
6. De Chermont, Q. L. M. et al. Nanoprobes with near-infrared persistent luminescence for in vivo imaging. *Proc. Natl Acad. Sci. USA* **104**, 9266–9271 (2007).
7. Maldiney, T. et al. The in vivo activation of persistent nanophosphors for optical imaging of vascularization, tumours and grafted cells. *Nat. Mater.* **13**, 418–426 (2014).
8. Li, Z. et al. Direct aqueous-phase synthesis of sub-10 nm "luminous pearls" with enhanced in vivo renewable near-infrared persistent luminescence. *J. Am. Chem. Soc.* **137**, 5304–5307 (2015).
9. Jiang, Y. et al. A generic approach towards afterglow luminescent nanoparticles for ultrasensitive in vivo imaging. *Nat. Commun.* **10**, 2064 (2019).
10. So, M.-K., Xu, C., Loening, A. M., Gambhir, S. S. & Rao, J. Self-illuminating quantum dot conjugates for in vivo imaging. *Nat. Biotechnol.* **24**, 339–343 (2006).
11. Shaffer, T. M., Pratt, E. C. & Grimm, J. Utilizing the power of Cerenkov light with nanotechnology. *Nat. Nanotechnol.* **12**, 106–117 (2017).
12. Xu, Y., Liu, H. & Cheng, Z. Harnessing the power of radionuclides for optical imaging: Cerenkov luminescence imaging. *J. Nucl. Med.* **52**, 2009–2018 (2011).
13. Lu, L. et al. NIR-II bioluminescence for in vivo high contrast imaging and in situ ATP-mediated metastases tracing. *Nat. Commun.* **11**, 4192 (2020).
14. Xie, C., Zhen, X., Miao, Q., Lyu, Y. & Pu, K. Self-assembled semiconducting polymer nanoparticles for ultrasensitive near-infrared afterglow imaging of metastatic tumours. *Adv. Mater.* **30**, 1801331 (2018).
15. Wu, L. et al. H_2S-activatable near-infrared afterglow luminescent probes for sensitive molecular imaging in vivo. *Nat. Commun.* **11**, 446 (2020).
16. He, S., Xie, C., Jiang, Y. & Pu, K. An organic afterglow protheranostic nanoassembly. *Adv. Mater.* **31**, 1902672 (2019).
17. Jiang, Y. & Pu, K. Molecular probes for autofluorescence-free optical imaging. *Chem. Rev.* **121**, 13086–13131 (2021).
18. Chen, H. et al. $LiGa_5O_8$: Cr-based theranostic nanoparticles for imaging-guided X-ray induced photodynamic therapy of deep-seated tumours. *Mater. Horiz.* **4**, 1092–1101 (2017).
19. Pei, P. et al. X-ray-activated persistent luminescence nanomaterials for NIR-II imaging. *Nat. Nanotechnol.* **16**, 1011–1018 (2021).
20. Chen, Y. et al. Ultra-high-frequency radio-frequency acoustic molecular imaging with saline nanodroplets in living subjects. *Nat. Nanotechnol.* **16**, 717–724 (2021).
21. Flannigan, D. J. & Suslick, K. S. Plasma formation and temperature measurement during single-bubble cavitation. *Nature* **434**, 52–55 (2005).
22. Ostrovskii, I., Korotchenkov, O., Goto, T. & Grimmeiss, H. Sonoluminescence and acoustically driven optical phenomena in solids and solid–gas interfaces. *Phys. Rep.* **311**, 1–46 (1999).
23. Wu, X. et al. Sono-optogenetics facilitated by a circulation-delivered rechargeable light source for minimally invasive optogenetics. *Proc. Natl Acad. Sci. USA* **116**, 26332–26342 (2019).
24. Fridman, W. H., Pages, F., Sautes-Fridman, C. & Galon, J. The immune contexture in human tumours: impact on clinical outcome. *Nat. Rev. Cancer* **12**, 298–306 (2012).
25. Van Elssen, C. H. et al. Noninvasive imaging of human immune responses in a human xenograft model of graft-versus-host disease. *J. Nucl. Med.* **58**, 1003–1008 (2017).
26. Grivennikov, S. I., Greten, F. R. & Karin, M. Immunity, inflammation, and cancer. *Cell* **140**, 883–899 (2010).
27. Szabó, C., Ischiropoulos, H. & Radi, R. Peroxynitrite: biochemistry, pathophysiology and development of therapeutics. *Nat. Rev. Drug Discov.* **6**, 662–680 (2007).
28. Wynn, T. A., Chawla, A. & Pollard, J. W. Macrophage biology in development, homeostasis and disease. *Nature* **496**, 445–455 (2013).
29. Huang, J., Jiang, Y., Li, J., Huang, J. & Pu, K. Molecular chemiluminescent probes with a very long near-infrared emission wavelength for in vivo imaging. *Angew. Chem. Int. Ed.* **60**, 3999–4003 (2021).
30. Su, X. et al. Interferon-γ regulates cellular metabolism and mRNA translation to potentiate macrophage activation. *Nat. Immunol.* **16**, 838–849 (2015).
31. Rodell, C. B. et al. TLR7/8-agonist-loaded nanoparticles promote the polarization of tumour-associated macrophages to enhance cancer immunotherapy. *Nat. Biomed. Eng.* **2**, 578–588 (2018).
32. Lester, S. N. & Li, K. Toll-like receptors in antiviral innate immunity. *J. Mol. Biol.* **426**, 1246–1264 (2014).

33. Friedman, A. A., Letai, A., Fisher, D. E. & Flaherty, K. T. Precision medicine for cancer with next-generation functional diagnostics. *Nat. Rev. Cancer* **15**, 747–756 (2015).
34. Chen, Q. et al. In situ sprayed bioresponsive immunotherapeutic gel for post-surgical cancer treatment. *Nat. Nanotechnol.* **14**, 89–97 (2019).
35. Smyth, M. J., Ngiow, S. F., Ribas, A. & Teng, M. W. Combination cancer immunotherapies tailored to the tumour microenvironment. *Nat. Rev. Clin. Oncol.* **13**, 143–158 (2016).
36. Sindrilaru, A. et al. An unrestrained proinflammatory M1 macrophage population induced by iron impairs wound healing in humans and mice. *J. Clin. Invest.* **121**, 985–997 (2011).
37. Klebanoff, C. A., Gattinoni, L. & Restifo, N. P. CD8$^+$ T-cell memory in tumor immunology and immunotherapy. *Immunol. Rev.* **211**, 214–224 (2006).
38. Van Manen, L. et al. A practical guide for the use of indocyanine green and methylene blue in fluorescence-guided abdominal surgery. *J. Surg. Oncol.* **118**, 283–300 (2018).
39. Huang, J., Huang, J., Cheng, P., Jiang, Y. & Pu, K. Near-infrared chemiluminescent reporters for in vivo imaging of reactive oxygen and nitrogen species in kidneys. *Adv. Funct. Mater.* **30**, 2003628 (2020).
40. Hanna, E., Abadi, R. & Abbas, O. Imiquimod in dermatology: an overview. *Int J. Dermatol.* **55**, 831–844 (2016).
41. Dumortier, G., Grossiord, J. L., Agnely, F. & Chaumeil, J. C. A review of poloxamer 407 pharmaceutical and pharmacological characteristics. *Pharm. Res.* **23**, 2709–2728 (2006).
42. Ouyang, J. et al. Ultrasound mediated therapy: recent progress and challenges in nanoscience. *Nano Today* **35**, 100949 (2020).
43. Canavese, G. et al. Nanoparticle-assisted ultrasound: a special focus on sonodynamic therapy against cancer. *Chem. Eng. J.* **340**, 155–172 (2018).
44. Rajamma, D. B., Anandan, S., Yusof, N. S. M., Pollet, B. G. & Ashokkumar, M. Sonochemical dosimetry: a comparative study of Weissler, Fricke and terephthalic acid methods. *Ultrason Sonochem.* **72**, 105413 (2021).
45. Zhao, P. et al. Aggregation-enhanced sonodynamic activity of phthalocyanine-artesunate conjugates. *Angew. Chem. Int. Ed.* **61**, e202113506 (2022).
46. Chao, Y. et al. Combined local immunostimulatory radioisotope therapy and systemic immune checkpoint blockade imparts potent antitumour responses. *Nat. Biomed. Eng.* **2**, 611–621 (2018).
47. van der Meel, R. et al. Smart cancer nanomedicine. *Nat. Nanotechnol.* **14**, 1007–1017 (2019).
48. Wang, C. et al. In situ activation of platelets with checkpoint inhibitors for post-surgical cancer immunotherapy. *Nat. Biomed. Eng.* **1**, 0011 (2017).
49. Xu, J. et al. A general strategy towards personalized nanovaccines based on fluoropolymers for post-surgical cancer immunotherapy. *Nat. Nanotechnol.* **15**, 1043–1052 (2020).
50. Ubil, E. et al. Tumor-secreted Pros1 inhibits macrophage M1 polarization to reduce antitumor immune response. *J. Clin. Invest.* **128**, 2356–2369 (2018).
51. Michaelis, K. A. et al. The TLR7/8 agonist R848 remodels tumor and host responses to promote survival in pancreatic cancer. *Nat. Commun.* **10**, 4682 (2019).
52. Schaap, A. P., Chen, T.-S., Handley, R. S., DeSilva, R. & Giri, B. P. Chemical and enzymatic triggering of 1,2-dioxetanes. 2: fluoride-induced chemiluminescence from tert-butyldimethylsilyloxy-substituted dioxetanes. *Tetrahedron Lett.* **28**, 1155–1158 (1987).

Acknowledgements

K.P. acknowledges financial support from the Singapore National Research Foundation (NRF) (NRF-NRFI07-2021-0005), and the Singapore Ministry of Education, Academic Research Fund Tier 1 (2019-T1-002-045, RG125/19, RT05/20) and Academic Research Fund Tier 2 (MOE-T2EP30220-0010).

Author contributions

K.P. conceived and designed the study. C.X. and Y.J. performed nanoparticle construction. C.X. performed in vivo experiments. J.H. performed the chemical synthesis. C.X., S.H. and C.Z. performed in vitro characterization and cell experiments. K.P. and C.X. analyzed the data and drafted the manuscript. All authors contributed to the writing of the manuscript.

Competing interests

The authors declare no competing interests.

Additional information

Supplementary information The online version contains supplementary material available at https://doi.org/10.1038/s41551-022-00978-z.

Correspondence and requests for materials should be addressed to Kanyi Pu.

Peer review information *Nature Biomedical Engineering* thanks the anonymous, reviewer(s) for their contribution to the peer review of this work.

Reprints and permissions information is available at www.nature.com/reprints.

nature portfolio

Corresponding author(s): Kanyi Pu

Last updated by author(s): Oct 28, 2022

Reporting Summary

Nature Portfolio wishes to improve the reproducibility of the work that we publish. This form provides structure for consistency and transparency in reporting. For further information on Nature Portfolio policies, see our Editorial Policies and the Editorial Policy Checklist.

Statistics

For all statistical analyses, confirm that the following items are present in the figure legend, table legend, main text, or Methods section.

n/a	Confirmed	
☐	☒	The exact sample size (*n*) for each experimental group/condition, given as a discrete number and unit of measurement
☐	☒	A statement on whether measurements were taken from distinct samples or whether the same sample was measured repeatedly
☐	☒	The statistical test(s) used AND whether they are one- or two-sided *Only common tests should be described solely by name; describe more complex techniques in the Methods section.*
☐	☒	A description of all covariates tested
☐	☒	A description of any assumptions or corrections, such as tests of normality and adjustment for multiple comparisons
☐	☒	A full description of the statistical parameters including central tendency (e.g. means) or other basic estimates (e.g. regression coefficient) AND variation (e.g. standard deviation) or associated estimates of uncertainty (e.g. confidence intervals)
☐	☒	For null hypothesis testing, the test statistic (e.g. *F*, *t*, *r*) with confidence intervals, effect sizes, degrees of freedom and *P* value noted *Give P values as exact values whenever suitable.*
☒	☐	For Bayesian analysis, information on the choice of priors and Markov chain Monte Carlo settings
☒	☐	For hierarchical and complex designs, identification of the appropriate level for tests and full reporting of outcomes
☒	☐	Estimates of effect sizes (e.g. Cohen's *d*, Pearson's *r*), indicating how they were calculated

Our web collection on statistics for biologists contains articles on many of the points above.

Software and code

Policy information about availability of computer code

Data collection	IVIS images were collected by Living Image 4.3 Software (Perkin Elmer). Flow-cytometry data were collected by FACS Diva software v6.0.
Data analysis	Fluorescence images were analysed using Living Image 4.3 Software (PerkinElmer) or ImageJ v1.51a Software. NMR spectra were analysed using Mestre Nova LITE v5.2.5-4119 software (Mestre lab Research S.L.). Statistical calculations were performed using GraphPad Prism 7.0. Flow-cytometry results were analysed by FlowJo v10.

For manuscripts utilizing custom algorithms or software that are central to the research but not yet described in published literature, software must be made available to editors and reviewers. We strongly encourage code deposition in a community repository (e.g. GitHub). See the Nature Portfolio guidelines for submitting code & software for further information.

Data

Policy information about availability of data

All manuscripts must include a data availability statement. This statement should provide the following information, where applicable:

- Accession codes, unique identifiers, or web links for publicly available datasets
- A description of any restrictions on data availability
- For clinical datasets or third party data, please ensure that the statement adheres to our policy

The main data supporting the results in this study are available within the paper and its Supplementary Information. Source data for the main figures are provided with this paper. The raw and analysed datasets generated during the study are too large to be publicly shared, yet they are available for research purposes from the corresponding author on reasonable request.

Field-specific reporting

Please select the one below that is the best fit for your research. If you are not sure, read the appropriate sections before making your selection.

☒ Life sciences ☐ Behavioural & social sciences ☐ Ecological, evolutionary & environmental sciences

For a reference copy of the document with all sections, see nature.com/documents/nr-reporting-summary-flat.pdf

Life sciences study design

All studies must disclose on these points even when the disclosure is negative.

Sample size	We used G*power analysis to ensure that sample sizes were sufficient for the statistics to have adequate power (over 80%).
Data exclusions	No data were excluded from the study.
Replication	All experiments were reproduced reliably.
Randomization	The cages of mice were randomly selected and then divided into experimental groups for further treatment.
Blinding	Investigators were blinded to group allocation during the experiments.

Reporting for specific materials, systems and methods

We require information from authors about some types of materials, experimental systems and methods used in many studies. Here, indicate whether each material, system or method listed is relevant to your study. If you are not sure if a list item applies to your research, read the appropriate section before selecting a response.

Materials & experimental systems

n/a	Involved in the study	
☐	☒	Antibodies
☐	☒	Eukaryotic cell lines
☒	☐	Palaeontology and archaeology
☐	☒	Animals and other organisms
☒	☐	Human research participants
☒	☐	Clinical data
☒	☐	Dual use research of concern

Methods

n/a	Involved in the study	
☒	☐	ChIP-seq
☐	☒	Flow cytometry
☒	☐	MRI-based neuroimaging

Antibodies

Antibodies used	All antibodies were purchased from Biolegend (USA) unless otherwise indicated. Antibody against CD16/32 (93, 1:50) was used to block non-specific binding. Antibodies against CD11b (M1/70, 1:200), F4/80 (BM8, 1:20) and iNOS (W16030C, 1:160) were used for M1-macrophage staining. Antibodies against CD45 (30-F11, 1:200), CD3 (17A2, 1:100) and CD8 (53-6.7, 1:100) were used for cytotoxic-T-cell staining. Antibodies against CD4 (RM4-5, 1:100) and FOXP3 (MF-14, 1:200) were used for Treg-cell staining. Antibodies against CD62L (MEL-14, 1:100) and CD44 (IM7, 1:20) were used for memory-T-cell staining. Antibodies against CD11c (N418, 1:100), CD80 (16-10A1, 1:50), and CD86 (A17199A, 1:50) were used for mature-dendritic-cell staining. Tumour slices were stained with antibodies against high mobility group box 1 (HMGB-1) (3E3, Alexa Fluor 488-labelled, 1:200, Biolegend), Caspase-3 (#9664, rabbit anti-mouse, 1:400, Cell Signalling Technology), and rabbit anti-mouse calreticulin (PA3-900, 1:200, Thermo Fisher Scientific). Alexa Fluor 488-conjugated secondary antibody (goat anti-rabbit, 1:500, Thermo Fisher Scientific) was used in caspase-3 and calreticulin staining.
Validation	All antibodies were commercially available and were validated by the supplier. https://www.biolegend.com/en-us/quality/product-development https://www.cellsignal.com/about-us/cst-antibody-validation-principles https://www.thermofisher.com/sg/en/home/life-science/antibodies/invitrogen-antibody-validation.html

Eukaryotic cell lines

Policy information about cell lines

Cell line source(s)	The 4T1 murine mammary carcinoma cell line, RAW 264.7 murine macrophage cell line and 3T3 mouse embryonic fibroblast cell line were purchased from American Type Culture Collection (ATCC).
Authentication	The cell lines were authenticated by the supplier using STR analysis.

Mycoplasma contamination	No contamination was detected by the supplier (according to Hoechst DNA stains, agar culture and PCR-based assays).
Commonly misidentified lines (See ICLAC register)	No commonly misidentified cell lines were used.

Animals and other organisms

Policy information about studies involving animals; ARRIVE guidelines recommended for reporting animal research

Laboratory animals	Female BALB/c mouse (5–6 weeks old) were purchased from InVivos Pte Ltd (Singapore).
Wild animals	The study did not involve wild animals.
Field-collected samples	The study did not involve samples collected from the field.
Ethics oversight	The animal experiments were performed in compliance with the Guidelines for Care and Use of Laboratory Animals of the Nanyang Technological University-Institutional Animal Care and Use Committee (NTU-IACUC), and approved by the Institutional Animal Care and Use Committee (IACUC) for Animal Experiment, Singapore. Mice were group-housed in ventilated clear plastic cages under appropriate ambient temperature (~22°C), humidity (50%), and standard 12 h:12 h light:dark conditions.

Note that full information on the approval of the study protocol must also be provided in the manuscript.

Flow Cytometry

Plots

Confirm that:

☒ The axis labels state the marker and fluorochrome used (e.g. CD4-FITC).

☒ The axis scales are clearly visible. Include numbers along axes only for bottom left plot of group (a 'group' is an analysis of identical markers).

☒ All plots are contour plots with outliers or pseudocolor plots.

☒ A numerical value for number of cells or percentage (with statistics) is provided.

Methodology

Sample preparation	Tumours were dissected and digested with collagen I (2 mg mL-1), collagen IV (2 mg mL-1) and DNase I (0.2 mg mL-1) prepared in DMEM culture medium in 37°C water bath. Digested tissues were then incubated with red-blood-cell lysis buffer (420301, Biolegend) for 5 min, followed by passing through a 100-µm mesh strainer (352360, Falcon). Spleens were dissected and incubated with red-blood-cell lysis buffer to remove red blood cells. Single-cell suspensions were obtained and stained with antibodies according to the manufacturer's protocols, and then analysed by flow cytometry.
Instrument	Fortessa X20 (BD Biosciences)
Software	FACS Diva v6.0 and FlowJo v10.
Cell population abundance	No cell sorting was performed.
Gating strategy	In general, cells were first gated on FSC/SSC. Single cells were gated using FSC-H and FSC-A. Dead cells were excluded and further surface and intracellular antigen gating was performed on the live-cell population.

☒ Tick this box to confirm that a figure exemplifying the gating strategy is provided in the Supplementary Information.